

POLITECNICO DI TORINO

Master's Degree in Aerospace Engineering



Master's Degree Thesis

Analysis of small-scale rotors using CFD: protocol for the creation of a numerical database.

Supervisors

Prof. Domenic D'Ambrosio

Prof. Manuel Carreño Ruiz

Candidate

Paolo Sieni Miceli

October 2023

Summary

In this thesis, small-scale rotors will be analyzed using the CFD solver embedded in Star-CCM+. We will create a protocol that allows us to generate, from some input data, different geometries that will later be analyzed in a hovering condition and compared with a target geometry. The goal of the study is to validate the entire analysis process, from geometry creation to numerical analysis, setting the basis for the creation of a larger numerical database.

Chapter 1 is an introductory section to the thesis, highlighting the advantages of having a robust computational model under the given conditions. Chapter 2 includes a comprehensive discussion of the reduced-order models commonly used for simplified propeller analysis, introducing the main parameters that we will study in the simulations.

Chapter 3 illustrates the code used for generating various geometries, accompanied by a list of specific geometries that will be analyzed with Star CCM+. Chapter 4 discusses the methodology adopted in order to solve the rotating flow around the blade, while the next chapter, Chapter 5, outlines the complete procedure undertaken to develop the CFD model, which is going to be used, and the results obtained for the target geometry.

In Chapter 6, we will analyze the different geometries studied throughout the thesis.

Acknowledgements

Giunto alla fine di questo lungo percorso di studio vorrei dedicare queste pagine a tutte le persone che mi sono state vicine in questi anni e che mi hanno permesso di completare questo difficile e faticoso tragitto.

Vorrei ringraziare il professor Domenic D'Ambrosio che mi ha permesso di compiere questa attività di tesi e che ,con il suo corso, mi ha introdotto nel mondo dell'analisi computazionale.

Un grande ringraziamento va Manuel che in questi mesi mi ha seguito e mi ha offerto il suo aiuto e tutte le sue conoscenze. Lo ringrazio specialmente per la sua enorme disponibilità e pazienza durante tutto la fase di svolgimento dell'attività e per tutti gli aiuti e indicazioni che mi ha dato su come svolgere un corretta simulazione fluidodinamica.

Ringrazio la mia famiglia che mi ha permesso con i loro sacrifici di studiare e vivere in questi anni a Torino. Un grande grazie va a mia madre che in questi anni ha spesso sacrificato se stessa per aiutarmi a raggiungere questo traguardo e a mio padre che ci ha sempre creduto e per il continuo sostegno morale che mi ha offerto nei momenti di crisi. Ringrazio infine mio fratello con cui sono cresciuto e ho passato la maggior parte del tempo durante questi 25 anni. Ricordati che il tuo fratellino ti vuole tanto bene anche se non ti chiama spesso.

Ringrazio Giulia per essere stata al mio fianco in questi anni di università. Grazie per avermi staccato dalla scrivania e regalato momenti indimenticabili e per essere stata comprensiva tutte le altre volte che ti ho dato buca. Sei la mia luce nei momenti di crisi dove tutto fa male. Ti ringrazio per il supporto e l'amore che mi offri ogni giorno.

Ringrazio tutti i miei compagni di avventura e in particolare Enrico, Alessandro che hanno condiviso con me tutte le fatiche di questo percorso e con cui ho studiato e svolto la maggior parte dei progetti.

Un grazie anche a tutti i miei amici che mi hanno perso di mantenere un giusto equilibrio tra università ed vita sociale. Spero che il giorno della mia laurea siano presenti e pronti a festeggiare con me questo traguardo.

Ringrazio infine tutti i miei parenti e amici di famiglia.

Grazie Nonno Ciuzzo che mi ha fatto vedere la mia prima gara di Formula 1 in TV da cui tutto è partito e mia nonna Concettina che ha sempre creduto in noi nipoti. Spero che oggi mi guardiate da lassù con grande soddisfazione e gioia.

Table of Contents

List of Tables	IX
List of Figures	X
1 Introduction	1
2 Rotary-wing Aerodynamics	3
2.1 Actuator Disc Model	4
2.2 Simple impulsive theory	6
2.3 Extended Momentum Theory	8
2.4 Blade Element Theory	11
2.5 Blade Element Momentum Theory (BEMT)	13
2.6 Propeller Performance	16
3 Geometry Generation	17
3.1 Code Explanation	17
3.2 Constant chord blades	20
3.3 Variable chord blades	21
4 Mathematical Model	24
4.1 Moving Reference frame Approach	24
4.2 Turbulence modelling	26
4.2.1 Reynolds Average Navier-Stokes (RANS)	26
4.2.2 $k-\omega$ Models	28
5 Test Case:Blade P5-D15-S0.1	29
5.1 Fluid Domain	29
5.2 Boundary Condition and Interface	31
5.3 Grid Generation	32
5.3.1 Baseline mesh	32
5.4 Adaptive mesh refinement (AMR)	36

5.4.1	Q-Criterion	37
5.4.2	Field Functions Definitions	37
5.4.3	Refine mesh options	39
5.5	Blade P5-D15-S0.1	40
5.6	Solver Convergence	41
5.7	Performance Analysis	43
5.8	Qualitative data	47
5.9	Mesh independence study	51
6	Effects of geometric variations on blade performance	54
6.1	Effect of the solidity	54
6.1.1	Comparison of aerodynamic parameters	56
6.1.2	Qualitative Data	59
6.2	Effect of the pitch	62
6.2.1	Comparison of aerodynamic parameters	63
6.2.2	Qualitative Data	66
6.3	Effect of the cord distribution change	68
6.3.1	Comparison of aerodynamic parameters	69
6.3.2	Qualitative Data	72
7	Conclusion	74
	Bibliography	75
A	Constant Chord Code	77
B	Variable Chord Code	79

List of Tables

3.1	Example of geometry matrix [4]	17
3.2	List of geometries tested during the research	23
5.1	Surface Controls	33
5.2	Prism Layer settings	36
5.3	Prism Layer Mesher controls	36
5.4	Surface refinement	39
5.5	Prism Layer refinement	39
5.6	Performance value of P5-D15-S0.1	43
6.1	Performance change with solidity (baseline in yellow)	56
6.2	Change in Power required with solidity	57
6.3	Performance change with pitch angle (baseline in yellow)	63
6.4	Change in Power required with pitch	64
6.5	Performance change with changing in the chord distribution	69
6.6	Power variation with the chord distribution	70

List of Figures

1.1	Example of application [1]	1
2.1	Model of the blade	4
2.2	Model of the simple impulsive theory	6
2.3	Model of the extended momentum theory [2]	8
2.4	Annular differential control volume for EMT [2]	9
2.5	Model of the Blade Element Theory [4]	11
2.6	Model of the Blade Element Momentum Theory [4]	13
2.7	Iterative process [2]	15
3.1	Example of Data input	18
3.2	Pitch of the rotor	19
3.3	Example of pitch corrections	20
3.4	Example of chord distribution with a peak at 25%	22
3.5	Example of constant chord blade	22
3.6	Example of variable chord blades	23
4.1	Coordinate system in static and rotating frames of reference	25
5.1	Fluid Domain	29
5.2	Outer region	30
5.3	Inner region	30
5.4	External region Boundary conditions	31
5.5	Inner region Boundary conditions	32
5.6	Detail of the mesh result after controls	34
5.7	Detail of the prism layer	35
5.8	Field functions Applications	38
5.9	Adaptive mesh effect	38
5.10	Blade P5-D15-S0.1	40
5.11	Residuals convergence	41
5.12	Thrust convergence	42
5.13	Torque convergence	42

5.14	Thrust distribution per unit length	43
5.15	Torque distribution per unit length	44
5.16	Tip vortex visualization	44
5.17	Low-pressure zone at the tip of the blade	45
5.18	Comparison of pressure distribution in two blade sections	45
5.19	T/Q distribution per unit length	46
5.20	Isosurface Q-Criterion $5000/s^2$	47
5.21	Q-criterion Y-section at 0.00 m and 0.04 m	47
5.22	Q-criterion Y-section	48
5.23	Wall Shear Stress	49
5.24	Cell Relative Velocity streamlines on the blade with separation detail	49
5.25	Detail of the downstream wake	50
5.26	Effect of mesh variations on the Thrust	51
5.27	Effect of mesh variations on the Torque	52
5.28	Effect of mesh on Thrust distribution	52
5.29	Effect of mesh on Torque distribution	53
5.30	Effect of mesh on T/Q distribution	53
6.1	Blade-solidity 0.05	55
6.2	Blade-solidity 0.15	55
6.3	Change of Thrust distribution with solidity	57
6.4	Change of Torque distribution with solidity	58
6.5	Change in T/Q distribution with solidity	58
6.6	Comparison vortex structure Isosurface $Q=5000/s^2$	59
6.7	Comparison vortex structure $Y=0.0$ m	60
6.8	Comparison vortex structure $Y=0.04$ m	61
6.9	Blade-pitch 7	62
6.10	Blade-pitch 10	62
6.11	CL vs alpha	63
6.12	Change of thrust distribution with pitch	64
6.13	Change of torque distribution with pitch	65
6.14	Change in T/Q distribution with pitch	65
6.15	Difference region of separation	66
6.16	Comparison vortex structure $Q=5000/s^2$	66
6.17	Comparison vortex structure $Y=0.0$ m	67
6.18	Blade p5-d15-s0.1 with chord peak near the 25%	68
6.19	Blade p5-d15-s0.1 with chord peak near the 50%	69
6.20	Change of thrust distribution with chord distribution	70
6.21	Change of torque distribution with chord distribution	71
6.22	Change in T/Q distribution with chord	71
6.23	Comparison vortex structure Isosurface $Q=5000/s^2$	72

6.24 Comparison vortex structure $Y=0.0$ m	73
--	----

Chapter 1

Introduction

Propeller-based propulsion systems have a rich history of use in both the maritime and aeronautical domains. Initially, these systems were primarily employed in large-scale applications. However, in recent decades, there has been a substantial proliferation in the utilization of smaller devices, such as Unmanned Aerial Vehicles (UAVs) and drones, across various industries.

Just take, for instance, the burgeoning drone market, where these aerial devices have witnessed widespread adoption across a diverse range of sectors. Nowadays, drones play crucial roles in fields such as safety, land surveillance, emergency response, agriculture and even for recreational enthusiasts. This recent surge can be attributed to the significant reduction in material costs, a factor that has further fueled the popularity of these versatile machines.



Figure 1.1: Example of application [1]

The rapid expansion of the drone market has consequently led to the demand for effective techniques to accurately predict rotor performance. One of the most efficient means of assessing the performance of small-scale propellers is undoubtedly based on experimental testing within controlled wind tunnels. However, this method becomes impractical in terms of both cost and possibly results, particularly during the early stages of a project, due to the necessity of replicating specific environmental conditions and producing multiple blade prototypes.

A viable alternative for evaluating the flow field around a rotating blade is the utilization of Computational Fluid Dynamics (CFD) simulations. This approach offers numerous advantages, with the primary one being simplified and less resource-intensive geometric modeling. This, in turn, allows the reduction of the number of physical prototypes needed for testing in the wind tunnel.

Throughout my thesis work, I concentrated my efforts on designing a standardized protocol that enables the testing of different geometric rotor configurations with a remarkable level of accuracy, all within a relatively brief timeframe and with minimal direct intervention from an operator.

This procedure will be employed to construct a comprehensive numerical database that will facilitate the assessment of how alterations of geometric parameters impact both the performance and the intricate vortex patterns generated through the interplay between the flow and the blade.

In order to attain this outcome, the following components have been developed:

1. A code that enables the generation of different rotor geometries based on input data furnished by the operator.
2. A robust simulation setup that ensures a convergence with an adequate spatial resolution.

Chapter 2

Rotary-wing Aerodynamics

In recent years, Computational Fluid Dynamics (CFD) analyses have made significant advancements, resulting in improved solutions by either fully or partially resolving the Navier-Stokes equations while considering many more aspects of the problem.

Nevertheless, simplified techniques have not been entirely discarded. This happens because sophisticated analysis tools are not always readily available. In addition, there is often a preference for obtaining approximate data in order to avoid excessive computational expenses, particularly during the initial stages of the design process.

Analyzing the aerodynamic performance of a rotor blade is complex due to different factors:

1. the rotational motion of the blade
2. the change of rotor's geometry along the sections
3. the reduced Reynolds number that varies along the radial coordinates

In order of complexity, the most common reduced-order models are the Actuator Disc Model, Simple impulsive theory, Extended Momentum Theory, and the Blade Element Momentum Theory [2] [3].

The difference between them is related to the "approximations" that are made in the model.

2.1 Actuator Disc Model

The disk model allows us to greatly simplify the problem if we give up on knowing exactly the momentum field near the propeller.

The theory rests upon the following assumptions:

- the rotor is substituted by a permeable disc, with the same diameter as the blade, which lets the external rotational forces generate the motion.
- the fluid is inviscid, stationary, irrotational with an asymptotic velocity equal to V_∞
- pressure jump throughout the disc

Moreover, due to the different energy of the flow between the downstream of the disc and the external flow, the growth of a contact discontinuity, known as the wake of the blade, is possible.

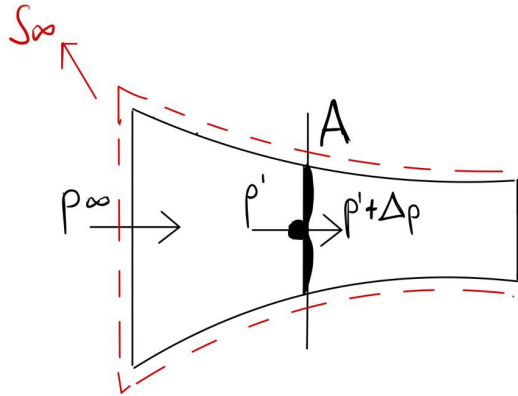


Figure 2.1: Model of the blade

We define the mean pressures upstream and downstream of the disk with p' and $p' + \Delta p$, respectively, and we apply the Momentum Balance Equation to the volume enclosed between the surface S_∞ and A where A is the area of the actuating disk while S_∞ is the surface enclosing the entire field of the motion.

$$\int_{S_\infty} (p\underline{\underline{I}} + \rho \underline{\underline{V}} \underline{\underline{V}}) \cdot \underline{\underline{n}} dS - \Delta p A \underline{\underline{k}} = 0 \quad (2.1)$$

The thrust exerted on the disc is equal to:

$$T = \Delta p A \quad (2.2)$$

Applying the Continuity equation to the stream tube we can express the flow rate as follows:

$$\dot{m} = \rho V_\infty A_m = \rho V_j A_j \quad (2.3)$$

where A_m is the section upstream while A_j is the section downstream.

Finally, if we combine the equation 2.2 and 2.3 and decompose the outer surface in $S_\infty = S_{\infty ext} + A_j + A_m$, the thrust can be express as:

$$T = \bar{k} * \int_{S_{\infty, ext}} [(p - p_\infty) \bar{n} + \rho \bar{V} \bar{V} \bar{n}] dS + \dot{m} (V_j - V_\infty) + (p_j - p_\infty) A_j \quad (2.4)$$

In the equation 2.4 we identify three contributions: the first one is the flow through the lateral surface while the other two are the components concerning the upstream and downstream of the control volume.

The integral term can be eliminated since it is possible to consider the lateral surface as a surface of current, for which the momentum flux is zero. The pressure term is also null since the integral at infinity is of order $\frac{1}{r^2}$. With these assumptions the equation 2.4 becomes:

$$T = \dot{m} (V_j - V_\infty) + (p_j - p_\infty) A_j \quad (2.5)$$

2.2 Simple impulsive theory

The first theory based on the actuator disk model was developed by Rankine.

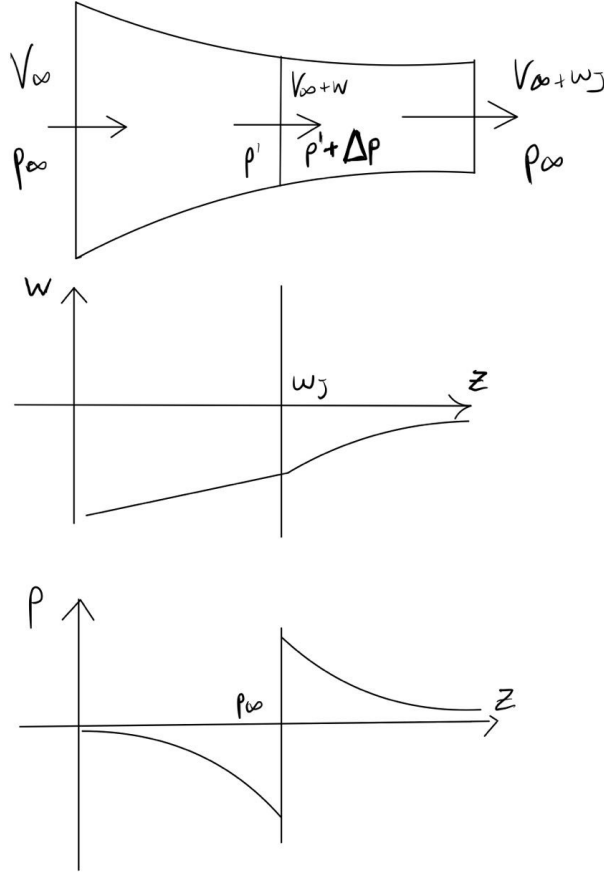


Figure 2.2: Model of the simple impulsive theory

In this theory, we will assume that the physical properties within the flow channel are exclusively dependent on the coordinate z . Moreover we will neglect variations in the radial and tangential directions. As a consequence, the disk remains unaffected by rotational forces, leading to the condition where $p_j = p_\infty$, resulting in the cancellation of the pressure term in equation 2.5.

By indicating the velocity of the disk and the infinitely downstream ones with $V_\infty + w$ and $V_\infty + w_j$, if the irrotationality conditions are valid, Bernoulli's theorem can be applied to the two portions of the flow tube separated by the disk.

$$p_\infty + \frac{\rho V_\infty^2}{2} = p' + \frac{\rho(V_\infty + w)^2}{2} \quad (2.6)$$

$$p' + \Delta p + \frac{\rho(V_\infty + w)^2}{2} = p_\infty + \frac{\rho(V_\infty + w_j)^2}{2} \quad (2.7)$$

Adding up the equations 2.6 and 2.7, the pressure jump induced by the rotor can be expressed as follows:

$$\Delta p = \rho w_j \left(V_\infty + \frac{1}{2} w_j \right) \quad (2.8)$$

By referring to equations 2.2 and 2.5, we obtain:

$$\Delta p = \rho w_j (V_\infty + w) \quad (2.9)$$

Comparing the two previous equations, we derive the fundamental result of this theory: **the axial velocity generated downstream of the propeller doubles the one generated on the disk.**

$$w_j = 2w \quad (2.10)$$

Hence, the Thrust, as a function of the velocity at the disk, can be expressed as follows:

$$T = 2\rho A(V_\infty + w)w \quad (2.11)$$

Consequently, the depiction of the model in Figure 2.2 remains coherent for a propeller in propulsion. In fact, when the thrust T is positive, the axial velocity will exhibit growth, leading to a streamlining contraction.

Applying the change in kinetic energy between upstream and downstream, the Power at the drive shaft can be estimated in the following way:

$$P = \dot{m} \left[\frac{1}{2} (V_\infty + w_j)^2 - \frac{1}{2} V_\infty^2 \right] = T (V_\infty + w) \quad (2.12)$$

Having derived the Thrust and rotor Power equations, we can now proceed to assess the performance of the propeller:

$$\eta = \frac{TV_\infty}{P} = \frac{1}{1 + a} \quad (2.13)$$

where $a = \frac{w}{v_\infty}$ is the axial inductor factor.

The 2.13 equation allows us to notice that the efficiency of the propeller depends only on the axial induction parameter. As a result, assigned the Thrust, **increasing the size of the blade will reduce the induction of the disk and increase the efficiency**. However, structural limitations should always be taken into account.

Lastly, if we discard the assumption of uniform axial induction along the helix ($w = w(r)$) and instead consider that each circular section operates independently without interaction with the others, we can directly employ the outcomes of simple impulsive theory to the individual circular sections:

$$dT = 4\pi r \rho V_\infty^2 (1+a) a dr; \quad T = 4\pi r \rho V_\infty^2 \int_0^R (1+a) a r dr \quad (2.14)$$

$$dP = 4\pi r \rho V_\infty^3 (1+a)^2 a dr; \quad P = 4\pi r \rho V_\infty^3 \int_0^R (1+a)^2 a r dr \quad (2.15)$$

2.3 Extended Momentum Theory

The simple impulsive theory was obtained by considering exclusively the axial velocity's effect while neglecting the variations of radial and rotational velocity. This extended theory introduced the blade rotation's effects with an additional component (v) which allows the theory to represent considerably better the fluid flow in the vicinity of the propeller.

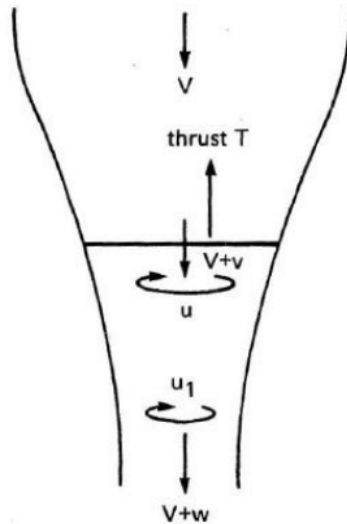


Figure 2.3: Model of the extended momentum theory [2]

As radial variations in velocity are present now the adequate volume of control to apply conservation laws would be an annular differential control volume enclosed by two stream tubes placed at r and $r+dr$ and two normal planes to the rotation axis placed at z and $z+dz$.

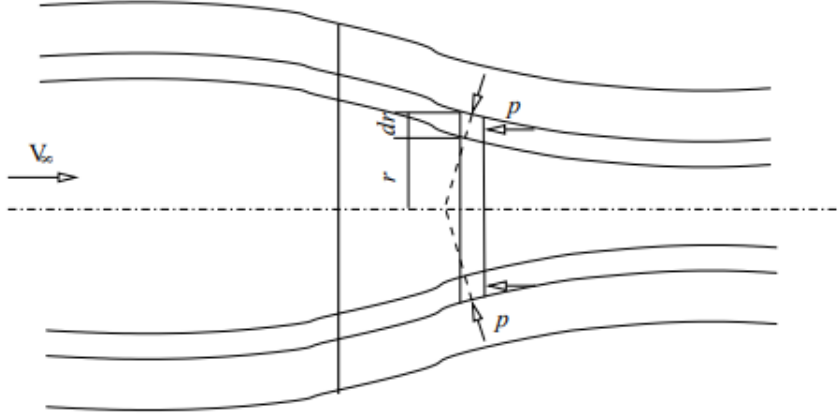


Figure 2.4: Annular differential control volume for EMT [2]

The steady-state angular momentum conservation equation can be written as:

$$\int_S \rho(\vec{r} \times \vec{V})\vec{V} \cdot \vec{n}dS + \int_S \vec{r} \times p\vec{n}dS = 0 \quad (2.16)$$

Since the pressure field is symmetrical for the axial axis of the blade, the pressure integral is zero and the only "non-zero" term is the convective flux of the two perpendicular surfaces to the axis.

By applying the conservation of the mass to the model, we obtain that:

$$\frac{\partial}{\partial z}(vr) = 0 \quad (2.17)$$

which integrated becomes:

$$vr = w^2r = \text{constant} \quad (2.18)$$

The change in angular velocity from 0 to w across the disk consequently implies the action of a torque dQ , which is equal to:

$$dQ = wr^2\rho VdA \quad (2.19)$$

Knowing that:

$$dA = 2\pi r dr \quad (2.20)$$

and introducing the rotational influence factor:

$$a' = \frac{w}{2\Omega} \quad (2.21)$$

which represents the kinetic energy lost due to the rotation of the fluid particles around the blade.

The torque can be expressed as:

$$dQ = 4\pi r^3 \rho V \Omega a' dr \quad (2.22)$$

Lastly, it is possible to define the power of the blade:

$$P = \int_0^R \Omega dQ = \int_0^R 4\pi r^3 \rho V \Omega^2 a' dr = a' \Omega^2 \rho V \pi R^4 = \dot{m} a' \Omega^2 R^2 \quad (2.23)$$

and efficiency:

$$\eta = \frac{TV_\infty}{P} = \frac{1 - a'}{1 + a'} \quad (2.24)$$

Relations 2.11, 2.22 and 2.24 are the fundamental equations of general impulsive theory.

2.4 Blade Element Theory

Even though the Extended Momentum theory can provide reliable preliminary data, it seems evident that, in order to design propeller blades, geometry has to be included. The blade element theory divides each blade into parts perpendicularly to the radial axis with the thickness dr , while the flow can be considered 2D in each element.

Let's consider one element dr at radial position r :

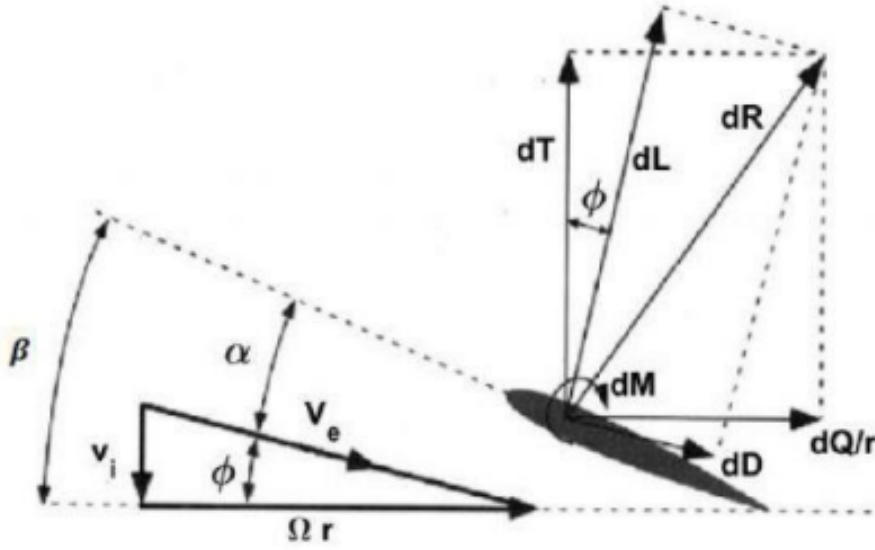


Figure 2.5: Model of the Blade Element Theory [4]

The pitch angle β can be evaluated as follows:

$$\beta = \alpha + \Phi \quad (2.25)$$

where α is the angle of attack, while Φ is the angle formed by the velocity triangle and is equal to:

$$\Phi = \arctan \frac{V_i}{\Omega r} \quad (2.26)$$

The relative velocity can be estimated from the triangle of velocity as follows:

$$|\vec{V}_e| = V_i \vec{e}_z + \Omega r \vec{e}_\theta = \sqrt{V_i^2 + (\Omega r)^2} \quad (2.27)$$

where V_i is the axial velocity.

Having defined the following parameters, we can now evaluate the aerodynamic forces acting on each radial element:

$$\delta L(r) = \frac{1}{2}\rho V_e(r)^2 c \delta r C_L(r) \quad (2.28)$$

$$\delta D(r) = \frac{1}{2}\rho V_e(r)^2 c \delta r C_D(r) \quad (2.29)$$

Looking at the figure, we can understand how to bind the expression of the aerodynamic forces with the Thrust, which is normal at the rotor plane:

$$\delta T(r) = \delta L \cos(\Phi(r)) + \delta D \sin(\Phi(r)) \quad (2.30)$$

$$\delta Q(r) = (\delta D \cos(\Phi(r)) + \delta L \sin(\Phi(r)))r \quad (2.31)$$

By integrating the expression 2.30 and 2.31 along the entire extension of the blade we obtain the value of Thrust and Power for each propeller blade:

$$T = N \int_0^R \delta T(r) dr \quad (2.32)$$

$$P = Nw \int_0^R \delta Q(r) dr \quad (2.33)$$

2.5 Blade Element Momentum Theory (BEMT)

As was previously pointed out, the main advantage of BET was the fact that it took into account the propeller geometry, however, it has the weakness of not being able to calculate the velocity induced at the disc. This issue can be overcome if we combine the "Blade Element Theory" with the "General Impulsive Theory" and set up an iterative solution. We also introduce the effects of the tangential velocity component through the tangential induction factor a' .

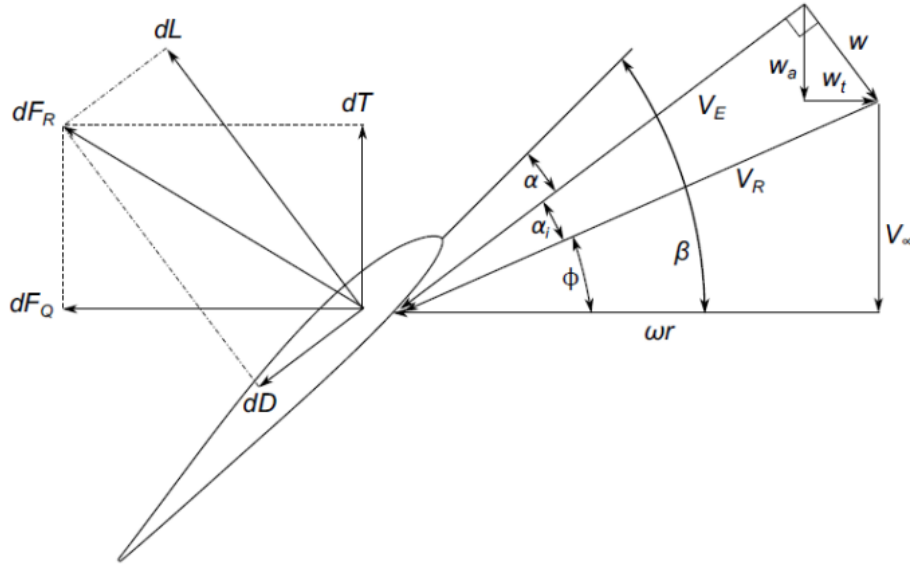


Figure 2.6: Model of the Blade Element Momentum Theory [4]

Let's recall the expression of the Lift and Drag of the wing profile:

$$L = \frac{1}{2} \rho V_{REL}^2 C_l c \quad (2.34)$$

$$D = \frac{1}{2} \rho V_{REL}^2 C_d c \quad (2.35)$$

The relationships between the aerodynamic parameters and the Thrust and Power are:

$$C_P = C_l \sin(\phi + \alpha_i) + C_d \cos(\phi + \alpha_i) \quad (2.36)$$

$$C_T = C_d \cos(\phi + \alpha_i) - C_l \sin(\phi + \alpha_i) \quad (2.37)$$

By integrating along the entire extension of the propeller and multiplying for the number of blades, such as 2.32 and 2.5, we obtain:

$$T = N \int_0^R \left[\frac{1}{2} \rho V_E^2 c C_l \cos(\phi + \alpha_i) - \frac{1}{2} \rho V_E^2 c C_d \sin(\phi + \alpha_i) \right] dr \quad (2.38)$$

$$P = N \omega \int_0^R \left[\frac{1}{2} \rho V_E^2 c C_l \sin(\phi + \alpha_i) + \frac{1}{2} \rho V_E^2 c C_d \cos(\phi + \alpha_i) \right] r dr \quad (2.39)$$

By taking into account the following relationships:

$$V_R^2 = V_\infty^2 + (\omega r)^2 \quad (2.40)$$

$$V_E^2 = V_R^2 \cos^2(\alpha_i) = (V_\infty^2 + (\omega r)^2) \cos^2(\alpha_i) \quad (2.41)$$

$$V_E \cos(\phi + \alpha_i) = V_\infty(1 + a) \quad (2.42)$$

$$V_E \sin(\phi + \alpha_i) = \omega r(1 - a') \quad (2.43)$$

the equations 2.38 and 2.39 can be written in their non-dimensional form:

$$C_T = \frac{\pi}{8} \int_{r_0}^R \left(J^2 + \pi^2 \left(\frac{r}{R} \right)^2 \right) \left(\frac{Nc}{\pi R} \right) \cos^2(\alpha_i) [C_L \cos(\phi + \alpha_i) - C_D \sin(\phi + \alpha_i)] dr \quad (2.44)$$

$$C_P = \frac{\pi}{8} \int_{r_0}^R \left(J^2 + \pi^2 \left(\frac{r}{R} \right)^2 \right) \left(\frac{Nc}{\pi R} \right) \cos^2(\alpha_i) [C_L \sin(\phi + \alpha_i) + C_D \cos(\phi + \alpha_i)] \frac{r}{R} dr \quad (2.45)$$

The angle α_i represents the first link between the two theories. The second one is derived by equalizing, in the iterative process, the Thrust and Power coefficients derived separately from the two different theories.

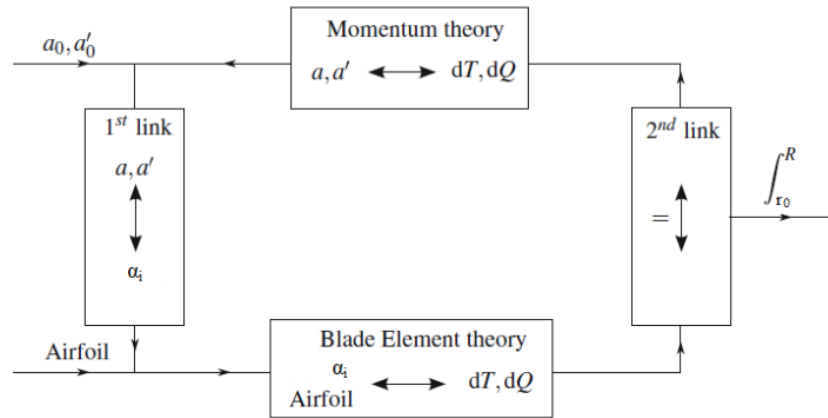


Figure 3.2: Blade element momentum method iteration loop.

Figure 2.7: Iterative process [2]

The iterative starts with the values of a and a' in order to derive the values of α_i . By noting this parameter, it is possible to calculate the aerodynamic performances (Thrust and Momentum), which are used to evaluate, with the Momentum Theory, the two assumed parameters and check if they coincide with the initial guest.

2.6 Propeller Performance

The propeller performance is dependent, apart from the geometry of the propeller, on the following parameters:

- Propeller diameter (D)
- Inflow velocity (V)
- Fluid density (ρ)
- Fluid dynamic viscosity (μ)
- Rotation rate (n)
- Speed of sound (a)

Carrying out a dimensional analysis, the performance depends only on three non-dimensional parameters:

- Advance ratio

$$J = \frac{V_\infty}{nD} \quad (2.46)$$

- Reynolds

$$Re = \frac{\rho n D^2}{\mu} \quad (2.47)$$

- Mach

$$M = \frac{nD}{a} \quad (2.48)$$

With this parameter, we can introduce the following non-dimensional coefficients:

- Thrust coefficient

$$C_T = \frac{T}{\rho \Omega^2 \pi R^4} \quad (2.49)$$

- Torque coefficient

$$C_Q = \frac{Q}{\rho \Omega^2 \pi R^5} \quad (2.50)$$

- Power coefficient

$$C_P = 2\pi C_Q \quad (2.51)$$

- Efficiency

$$\eta = \frac{J C_T}{C_P} \quad (2.52)$$

where $\Omega = [\text{rad/s}]$

The general performance of a propeller is usually defined by the functional curves $C_T = C_T(\mathbf{J}, \mathbf{Re}, \mathbf{M})$ and $C_Q = C_Q(\mathbf{J}, \mathbf{Re}, \mathbf{M})$.

Chapter 3

Geometry Generation

3.1 Code Explanation

The primary goal was to create a code capable of generating various geometry models. In order to achieve this result, a **macro** was utilized. The macro uses an Excel file that contains the profile positions section-by-section and automatically constructs the rotor blade within **Solidworks**. The code for generating the Excel file was developed in previous studies [4] and requires, as input data, a table containing the geometric information of the blade and Airfoil chosen.

r/R	c/R	Beta(°)	0.5 chord line(x-axis)	0.5 chord line(y-axis)
0.05	0.109	34.4349	0	0
0.15	0.109	37.9997	3.2544	2.3498
0.2	0.132	38.5861	3.1167	2.7324
0.25	0.155	36.9543	2.6233	2.8764
0.3	0.175	34.5594	2.0821	2.9998
0.35	0.192	32.0832	1.0286	3.0872
0.4	0.206	29.2839	0.0743	3.2204
0.45	0.216	26.3464	-0.6826	3.2369
0.5	0.222	23.5295	-1.3063	3.1419
0.55	0.225	21.3476	-2.1386	2.9216
0.6	0.224	19.6721	-2.7452	2.5133
0.65	0.219	18.1851	-3.3633	2.0663
0.7	0.21	16.8356	-3.8548	1.5921
0.75	0.197	15.2854	-4.5583	1.2267
0.8	0.18	14.0134	-4.9145	0.7775
0.85	0.159	12.8295	-5.3691	0.5116
0.9	0.133	11.7877	-5.7588	0.4309
0.95	0.1077	10.4528	-6.2914	0.3256
1	0.0100	9.0000	-11.2914	-0.7198

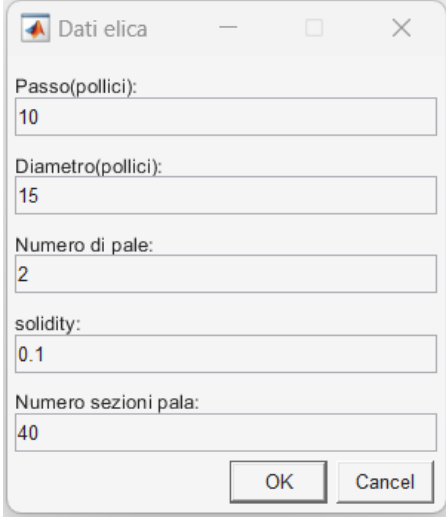
Table 3.1: Example of geometry matrix [4]

where:

- $\frac{r}{R}$ is the radial position for each section of the blade;
- $\frac{c}{R}$ is the cord distribution;
- β is the pitch angle;
- position of the quarter chord line.

Since we want to generate geometries without utilizing scans of existing blades, we need to find a method that allows us to determine the required parameters of the matrix for all the sections. Considering the data required, we decided to use parameters that are commonly used for commercial blade classification.

The data inputs utilized are the following:



The image shows a dialog box titled "Dati elica" with a standard Windows-style title bar (minimize, maximize, close buttons). The dialog contains five input fields, each with a label and a text box containing a value:

- Passo(pollici): 10
- Diametro(pollici): 15
- Numero di pale: 2
- solidity: 0.1
- Numero sezioni pala: 40

At the bottom right of the dialog are two buttons: "OK" and "Cancel".

Figure 3.1: Example of Data input

The first two parameters are used for the identification of the size of a propeller -e.g. "15 X 10"- and they indicate respectively the pitch and diameter of the rotor.

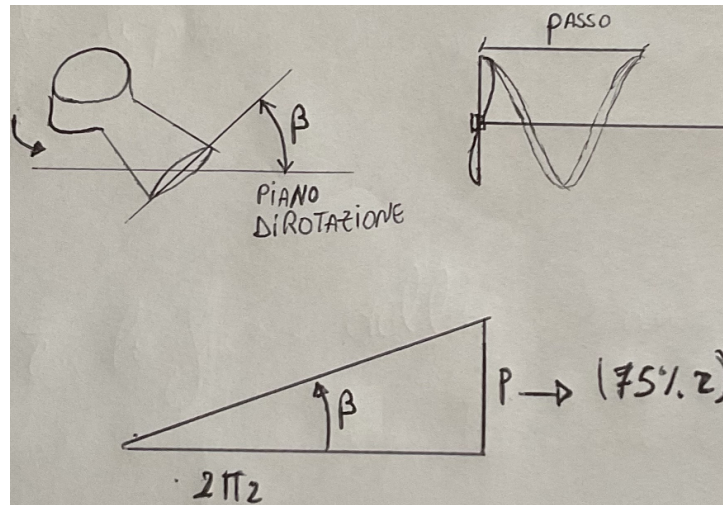


Figure 3.2: Pitch of the rotor

The diameter of the propeller is that of the outer disk, which is generated during rotation, while the pitch is the distance the propeller travels in one complete revolution. The pitch value is not constant due to the twisting of the blades near the hub so the value reported corresponds to 75% of the disk radius, referred to as conventional pitch.

The third and fourth parameters are used for the evaluation of **the chord distribution**.

The solidity is defined as the fraction of the annular area in the control volume, which is covered by blades. For a rotor with N blades, R radius and c chor, the rotor solidity is equal to:

$$\sigma = \frac{S_{rot}}{S_{disc}} = \frac{N c_{tip} 0.85}{\pi R} \quad (3.1)$$

The last data input is used to determine the number of sections in which we divide the blade.

In detail, two codes were created: one that generates geometries with fixed chords and the other with variable chords.

3.2 Constant chord blades

- The radial position of each section was determined by dividing a unit vector into the desired number of sections.
- The chord distribution was determined with the definition of solidity:

$$c_{tip} = \frac{\sigma R \pi}{N_{pale} 0.85} \quad (3.2)$$

where the value of 0.85 is due to the fact that the rotor section is not complete, considering that the first 15% of the blade is occupied by the hub.

Since the chord remains constant, the value that was estimated with 3.2 is the chord at the tip of the blade and it was subsequently assigned to each section along the blade's length.

- the pitch angle was calculated through the definition of the pitch:

$$\beta = \arctan\left(\frac{p}{2\pi r 0.75}\right) \quad (3.3)$$

Certainly, as the value of "r" decreases, the angle " β " tends to increase, potentially approaching infinity. In order to correct this problem, I approximated the value of β at the leading edge and then conducted an interpolation between this value and the others which were determined using equation 3.3.

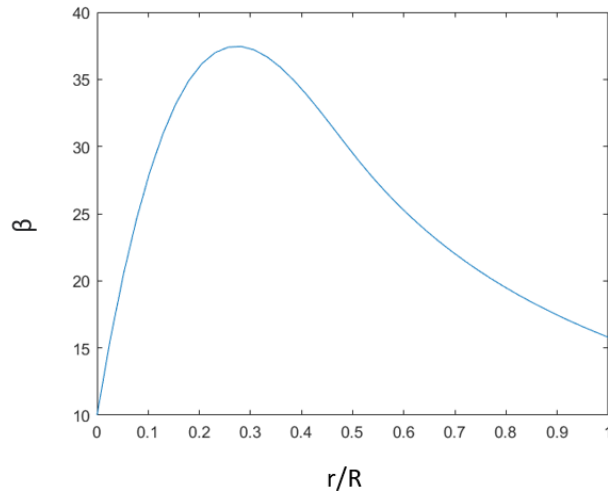


Figure 3.3: Example of pitch corrections

3.3 Variable chord blades

For these blade types, the radial position and pitch angle were determined in the same way discussed in 3.2.

For our initial study of the parameters, it was decided to examine two specific geometries. The first geometry aims for a relatively uniform chord distribution with a peak around half the radius to approximate an elliptical blade shape. The second geometry, on the other hand, aims to obtain a characteristic distribution with a peak near 25%.

First of all, we calculated the chord at the tip using the following equations:

$$\sigma = \frac{N_{pale} \int_{0.15R}^R c(r) dr}{\pi R^2} = \frac{c_{tip} N_{pale}}{\pi R} [\ln 1/r]_{0.15R}^R \quad (3.4)$$

Once the value to the tip has been determined, in order to obtain these two geometries, different formulations of $c(r)$ were employed:

- one involving the square root to relax the value of the distribution ($\sqrt{c/R}$)
- the other without it (c/R)

After establishing the two chord distributions, a correction was required, similar to the one carried out for the pitch angle. We assigned to the root of the blade the value of the chord of the tip and then performed an interpolation between this value and the two distributions, which were truncated at 50% and 25% of the blade length respectively.

An example of the correction is shown in the following picture:

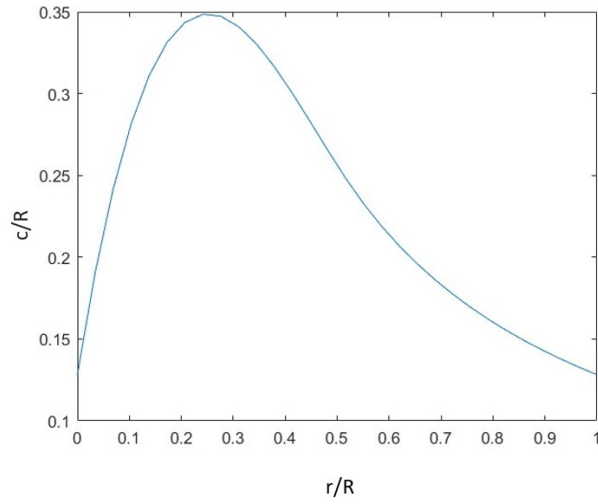


Figure 3.4: Example of chord distribution with a peak at 25%

After discussing the two codes, an example of both blades obtained is shown in the figures 3.5 and 3.6.

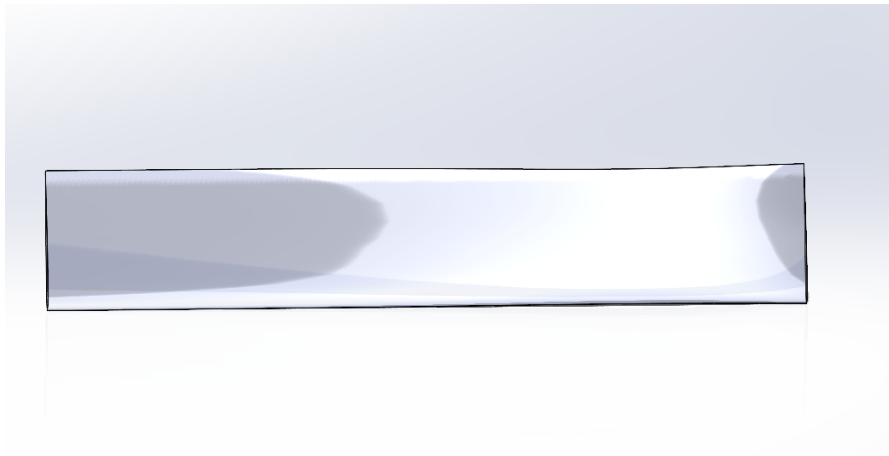


Figure 3.5: Example of constant chord blade

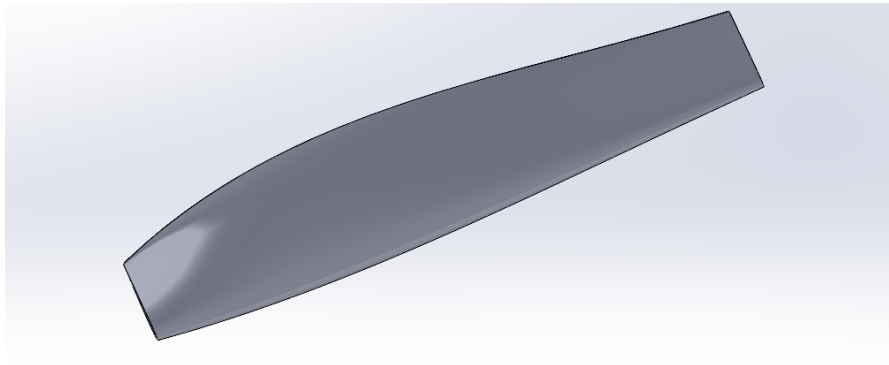


Figure 3.6: Example of variable chord blades

The following table shows the geometries that were created and tested with the analysis procedure. These blades will constitute our initial numerical database.

Blade	Pitch	Diameter	Solidity	N_section	V.Chord Dist.
P5_D15_S0.1	5	15	0.1	20	NO
P7_D15_S0.1	7	15	0.1	20	NO
P10_D15_S0.1	10	15	0.1	20	NO
P5_D15_S0.05	5	15	0.05	20	NO
P5_D15_S0.15	5	15	0.15	20	NO
P5_D15_S0.1_peak 50%	5	15	0.1	20	YES
P5_D15_S0.1_peak 25%	5	15	0.1	20	YES

Table 3.2: List of geometries tested during the research

Chapter 4

Mathematical Model

The main goal of this chapter is to give an overview of the method used to model rotating flows in Star CCM+. After that will present the turbulent model used in our analysis.

4.1 Moving Reference frame Approach

Among the available procedures that have been tested and validated, our decision ended up using a stationary approach, because it is optimal in the case of axisymmetric bodies and requires significantly less computational cost compared to the unsteady one [4],[5].

Constant rigid body motion can be solved using steady-state approaches, even though the flow field will be unsteady if we use a moving reference system, which can be either rotational or translational. If the moving elements are placed in a control volume associated with this non-stationary reference system, the time-averaged characteristics of the flow can be computed. Even more, in order to have reasonable results, the volume surrounding the rotating region must be axially symmetrical and the free-flow velocity should be parallel to the axis of rotation.

A change of reference system was hence adopted for the inner region so that the calculated quantities would be based on a rotating reference system centered on the propeller axis [6].

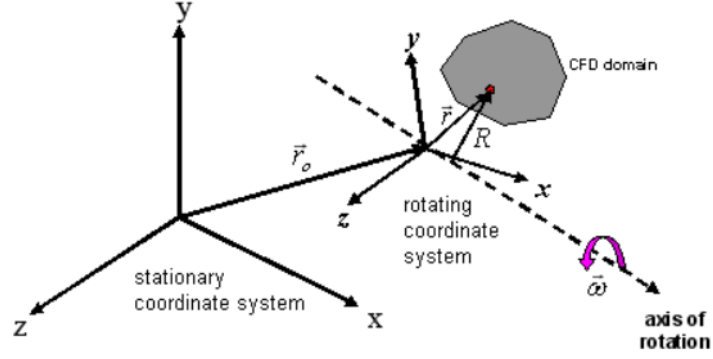


Figure 4.1: Coordinate system in static and rotating frames of reference [6]

In this system, the fluid velocity can be expressed as:

$$\vec{v} = \vec{v}_r + (\vec{\omega} \times \vec{r}) \quad (4.1)$$

where \vec{v} is the absolute velocity (velocity viewed from the stationary frame), \vec{v}_r is the relative velocity (velocity viewed from the rotating frame) and $(\vec{\omega} \times \vec{r})$ is "whirl" velocity (the velocity due to the moving frame).

The steady-state incompressible Navier-Stokes in conservative form can be expressed as:

$$\nabla \cdot (\rho \vec{v}) = 0 \quad (4.2)$$

$$\nabla \cdot (\rho \vec{v} \vec{v}) = -\nabla p + \mu \nabla \cdot \nabla(\vec{v}) \quad (4.3)$$

For the absolute velocity, the equations of Navier Stokes are:

$$\nabla \cdot (\rho \vec{v}) = 0 \quad (4.4)$$

$$\nabla \cdot (\rho \vec{v}_r \vec{v}) + \rho(\vec{\omega} \times \vec{V}) = -\nabla p + \mu \nabla \cdot \nabla(\vec{v}) \quad (4.5)$$

Ultimately, the governing equations for fluid flow within a consistently rotating frame, accounting for relative velocity, can be expressed as:

$$\nabla \cdot (\rho \vec{v}_r) = 0 \quad (4.6)$$

$$\nabla \cdot (\rho \vec{v}_r \vec{v}_r) = -\nabla p + \mu \nabla \cdot \nabla(\vec{v}_r) - \rho(2\vec{\omega} \times \vec{v}_r) - (\vec{\omega} \times \vec{\omega} \times \vec{r}) \quad (4.7)$$

The last two terms in the equation 4.7 are the Coriolis and Centripetal accelerations due to the non-inertial reference frame. It is important to point out that if the rotating domain is too small, the interfaces will be too close to the helix, and as a result, unphysical velocity distributions will be generated near the interfaces separating the two regions [6].

4.2 Turbulence modelling

While the boundary layer may exhibit laminar behavior, the Reynolds numbers present in our problem could generate a turbulent wake, which means that the turbulent scales must be solved to guarantee accurate results. STAR CCM+ provides 3 approaches: Reynolds-Averaged Navier-Stokes (RANS), Unsteady Reynolds-Averaged Navier-Stokes (URANS), and Large Eddy Simulation (LES) [7].

All three methods have their merits and demerits but we opted for the RANS approach to minimize computational costs. Additionally, it allowed us to use a steady-state approach while still achieving good accuracy in the results.

4.2.1 Reynolds Average Navier-Stokes (RANS)

RANS modeling originates from the Navier-Stokes equations. The average quantities of the variables are substituted into these equations and the resulting is averaged over time [4],[8].

In order to obtain these equations, Reynolds decomposition is performed:

$$\vec{u} = \vec{U} + \vec{u}' \quad (4.8)$$

$$p = \bar{P} + p' \quad (4.9)$$

$$T = \Phi + T' \quad (4.10)$$

In the stationary case, average magnitudes can be evaluated with a time average as follows:

$$\bar{U}(\vec{x}, t) = \frac{1}{2T_0} \int_{t-T_0}^{t+T_0} U(\vec{x}, t') dt' \quad (4.11)$$

In the process of time averaging, by definition, the time average of a fluctuating quantity is zero, so the obtained result is greatly simplified.

$$\bar{U}' \equiv \frac{1}{\Delta t} \int_{t_0}^{t_0+\Delta t} U' dt = 0 \quad (4.12)$$

The result equations are:

$$\nabla \cdot \vec{V} = 0 \quad (4.13)$$

$$\rho \nabla \cdot (\bar{V}\bar{V}) = -\nabla p + \nabla \cdot (\tau'_U - \rho \overline{u'u'}) \quad (4.14)$$

$$\rho C_P \vec{V} \nabla h = \nabla \cdot (K \nabla \vec{V} - \rho C_P \overline{T'V'}) \quad (4.15)$$

where:

$$\tau'_U = \mu [\nabla \vec{V} + (\nabla \vec{V})^T] \quad (4.16)$$

The effect of compressibility, field forces, and viscous dissipation terms have been neglected, as have the time-dependent terms since the simulation is steady.

The term $-\rho \overline{u'u'}$, known as the Reynolds stress tensor, is the mean flux of momentum due to turbulent fluctuations and its divergence appears as volumetric forcing of the mean flow. This term, which appears as unknown in the Reynolds equations, is determined by a turbulence model (closure problem), either via:

- the turbulent viscosity hypothesis
- the modeled Reynolds-stress transport equations.

Among the two approaches, the first is preferred for computational use because it is easier to apply and the computational cost required is lower compared to RST. The turbulent viscosity hypothesis is based on the analogy between the molecular diffusion process and turbulent motion.

We introduce the parameters μ_t , known as turbulent eddy viscosity, which allows us to express the stress tensor as a function of average quantities.

For the determination of the μ_t there are different approach:

- Spalart-Allmaras (1 equation)
- $k - \epsilon$ (2 equations)
- $k - \omega$ (2 equations)

The choice of the model was made by consulting the STAR CCM+ user's guide, which suggested the SST $k-\omega$ model, which is suitable for aerospace applications and advantageous in case of a mesh refinement process, which is essential for our application [7].

4.2.2 k- ω Models

The model attempts to predict turbulence by two partial differential equations for two variables, k , and ω , with the first variable being the turbulence kinetic energy (k) while the second ($\omega = \frac{k}{\epsilon}$) is the specific rate of dissipation.

The two additional balance equations that solve the two quantities are:

$$\frac{\partial k}{\partial t} + U_j \frac{\partial k}{\partial x_j} = \tau_{ij} \frac{\partial U_i}{\partial x_j} - \beta^* k \omega + \frac{\partial}{\partial x_j} \left[\left(\nu + \sigma^* \frac{k}{\omega} \right) \frac{\partial k}{\partial x_j} \right] \quad (4.17)$$

$$\frac{\partial \omega}{\partial t} + U_j \frac{\partial \omega}{\partial x_j} = \alpha \frac{\omega}{k} \tau_{ij} \frac{\partial U_i}{\partial x_j} - \beta \omega^2 + \frac{\sigma_d}{\omega} \frac{\partial k}{\partial x_k} \frac{\partial \omega}{\partial x_j} + \frac{\partial}{\partial x_j} \left[\left(\nu + \sigma \frac{k}{\omega} \right) \frac{\partial \omega}{\partial x_j} \right] \quad (4.18)$$

With these two quantities, the turbulent eddy viscosity can be derived by:

$$\mu_t = 0.009 \rho \frac{k}{\omega} \quad (4.19)$$

One of the advantages of this model concerns the possibility of being used on the entire boundary layer, but the disadvantage, on the other hand, is related to the fact that it is very sensitive to the variation of ω outside the boundary layer, which results in greater sensitivity to the boundary conditions of internal flows.

The k- ω model was subsequently improved and these problems were solved in the SST k- ω turbulence model [9], which exploits the wall advantage of the k- ω model and the insensitivity to boundary conditions of the k- ϵ model. A function is used to weigh the contributions of the two models as the distance from the wall changes.

Obviously, the computational cost increases slightly as it employs both methods but the SST k- ω model shows good behavior in adverse pressure gradients and separating flow [9].

Chapter 5

Test Case: Blade P5-D15-S0.1

This chapter will outline the simulation setup and the optimization procedure employed to attain a convergent configuration. Following the description of the experimental setup, we will present the results obtained for the P5-D15-S0.1 blade and analyze the impact of mesh variations on the outcomes.

5.1 Fluid Domain

During the first months of testing, a single-region configuration was tested. However, the main issue encountered was a highly unstable flow in the front area of the blade, significantly delaying the full development of the physical phenomenon and compromising solution convergence. For this reason, we decided to revert our approach to the two-region one.

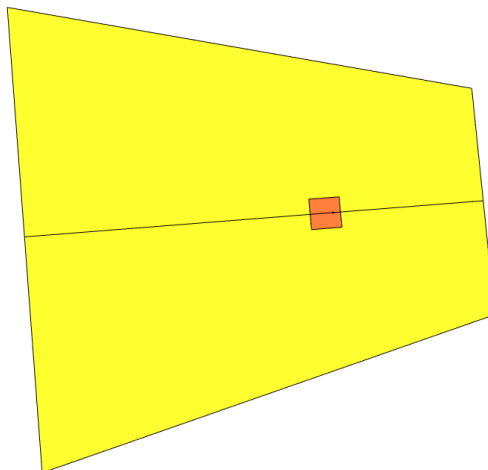


Figure 5.1: Fluid Domain

The outer region will be solved in a steady reference frame. The choice to use a steady-state approach, as explained in 4, implies that the computational domain must also be axisymmetric. For the shape, a conical one was chosen in order to limit possible flow reversals.

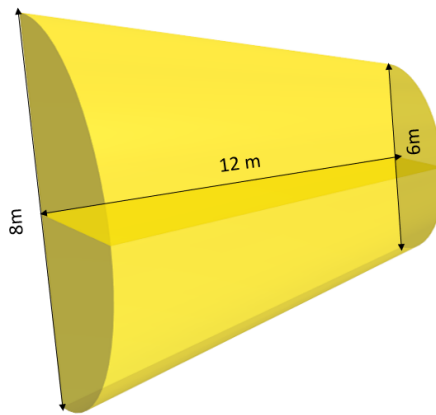


Figure 5.2: Outer region

For the inner region, we change reference systems and solve on a rotating reference frame that moves with the helix. This allows, as seen in 4.1, to use a stationary solver while maintaining unstable phenomena within the rotating.

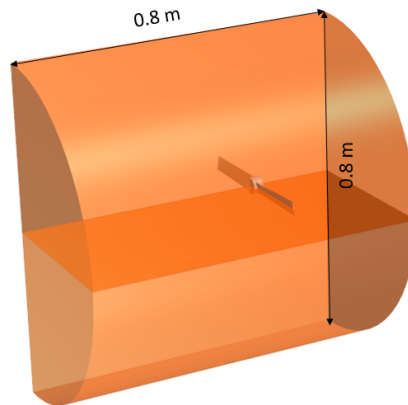


Figure 5.3: Inner region

5.2 Boundary Condition and Interface

A system of direct interfaces, underlined with the blu color, was used to connect the two reference systems, allowing quantities to be transmitted from the rotating system outward. This obviously requires that the rotating domain be large enough in order for the internal flow to develop.

An additional advantage of this method, which is also favorable for our purpose, is related to the possibility of using a periodic interface. This allows everything coming out from one region to be replicated in the input of another. This interface feature enabled us to cut the computational domain in half, leading to a significant reduction in simulation time. As for the results, we will simulate them for the motion of a single-bladed propeller, and then they will be adjusted according to the number of blades it consists of.

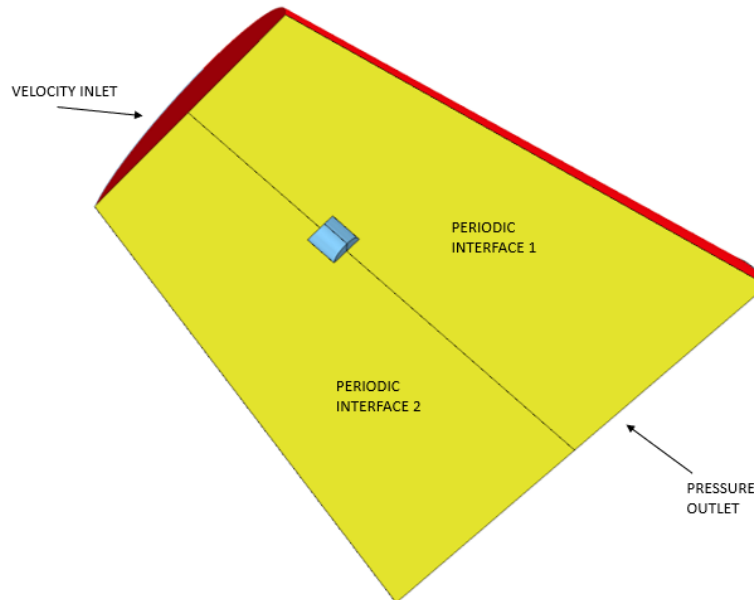


Figure 5.4: External region Boundary conditions

Regarding the boundary conditions, both an inlet and outlet condition were applied to the external domain.

At the inlet, a predefined velocity value was assigned. This decision was made due to the occurrence of counter-rotating vortices at the blade tip when simulating a propeller in a hovering state. This vortex, once detached from the blade, does not become entrained by the downstream external flow but it persists in its original

position and progressively expands. The assigned velocity has an axial component and is set to a low value of 0.1 m/s aims to accelerate the convergence. At the outlet, a pressure condition was applied, keeping the default conditions assigned by STAR-CCM+.

For the inner region, we assigned to rotational reference a rotation of 3000 RPM.

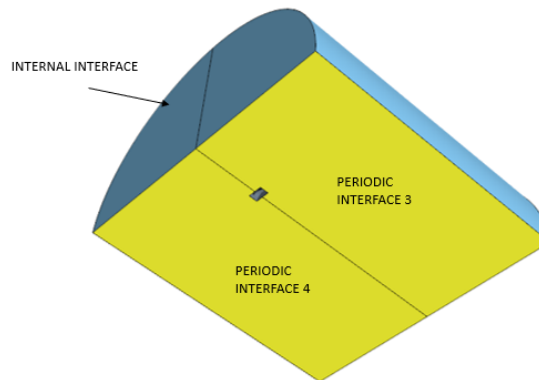


Figure 5.5: Inner region Boundary conditions

5.3 Grid Generation

In order to capture the flow that interacts with our blade, it was necessary to create a mesh optimization process, carried out in the following stages:

1. Baseline mesh generation
2. Two iterations of adaptive mesh refinement plus slight mesh refinement
3. Massive refinement in the area within the rotating domain

5.3.1 Baseline mesh

Simcenter STAR-CCM+ contains different types of meshing models that can be used to generate a volume mesh, starting from a suitably prepared surface.

The five types of meshing models are:

- Tetrahedral: tetrahedral cell shape-based core mesh
- Polyhedral: arbitrary polyhedral cell shape-based core mesh
- Trimmed: trimmed hexahedral cell shape-based core mesh
- Advancing Layer Mesh: polyhedral core mesh, with in-built prismatic layers that advance inward from a polygonal surface mesh.

Among all these methods, the **polyhedral grid** was chosen because it gives the possibility of performing adaptive refinement by choosing cell sizes, which was found to be crucial to vortex complete development [7].

Polyhedral Mesh

In the following section, the surface parameters assigned to each element belonging to the fluid domain will be presented for the baseline grid case:

Base size	4 m
Custom control: External Domain	Target Surface Size: 4%,0.16 m Minimum Surface Size: 2%,0.08 m
Custom control: Internal Domain	Target Surface Size: 2%, 0.08 m Minimum Surface Size: 1%,0.04 m
Custom control: Blade's Hub	Target Surface Size: 0.5%, 0.02 m Minimum Surface Size: 0.05%, 2 e-3 m
Custom control: Blade's Tip	Target Surface Size: 0.0075%, 3e - 4 m Minimum Surface Size: 0.005%, 2e-4 m
Custom control: Blade	Target Surface Size: 0.1%, 4e - 3 m Minimum Surface Size: 0.01%, 4e-4 m

Table 5.1: Surface Controls

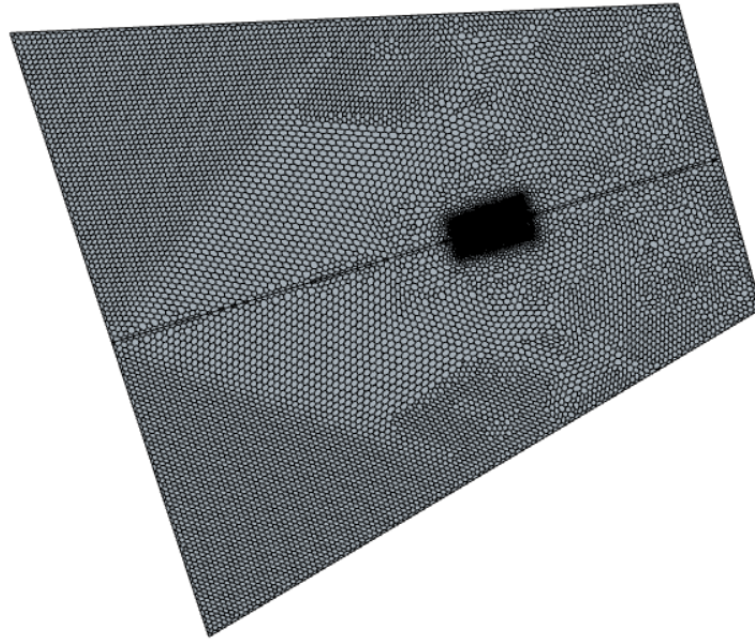


Figure 5.6: Detail of the mesh result after controls

Prism Layer Mesher

In order to solve appropriately the boundary layer of the blade, it is necessary to include a prism layer in the near wall region. STAR CCM+ allows three kinds of wall treatments [7]:

- "**Low y^+ treatment**", is equivalent to the traditional low Reynolds number approach. This method tries to resolve the viscous sublayer and requires a sufficiently fine mesh with near-wall cells located at y^+ of around unity.
- "**High y^+ treatment**", which models with wall functions up to the buffer layer and attempts to solve the logarithmic layer
- "**All y^+ treatment**" uses blended wall functions that emulate the low y^+ wall treatment for fine meshes, and the high y^+ wall treatment for coarse meshes.

In this case, the choice fell on the last one since it is assigned as the default by the STAR CCM+ chosen turbulence model. In order to achieve this, it is essential to determine the "prism layer near wall thickness" to ensure that the normalized height of the first cell is below $y^+ = 1$.

The following equations were used for estimating this parameter:

$$Re = \frac{\rho \cdot \Omega \cdot L_{\text{boundary layer}}}{\mu} \quad (5.1)$$

$$C_f = [2 \log_{10} (Re_x) - 0.65]^{-2.3} \quad \text{for } Re_x < 10^9 \quad (5.2)$$

$$\tau_w = C_f \cdot \frac{1}{2} \rho U_{\text{freestream}}^2 \quad u_* = \sqrt{\frac{\tau_w}{\rho}} \quad (5.3)$$

$$y = \frac{y^+ \mu}{\rho u_*} \quad (5.4)$$

Freestream Velocity	60 m/s
Density	1.225 kg/m ³
Dynamic Viscosity	1.82 e-5 kg/ms
Boundary layer length	0.1905 m
Desired Y+ value	1

Through the following formulas, the obtained value for the height of the first cell at the wall was equal to:

$$\Delta s = 6e^{-6} \text{ m} \quad (5.5)$$

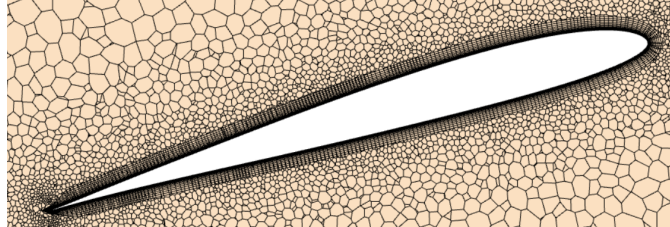


Figure 5.7: Detail of the prism layer

The prism layer settings are shown in Table 5.2, while the prism layer controls applied to the parts of the propeller are shown in Table 5.3.

Stretching function	Hyperbolic Tangent
Stretching Mode	Wall Thickness
Minimum Thickness Percentage	0.01
Layer percentage Reduction	0.0

Table 5.2: Prism Layer settings

Base size	4 m
Custom control: Blade's Hub	Number of prism layer: 10 Prism layer Near wall thickness: 6.2 e-6 m Prism layer total thickness: 0.01%,4 e-4 m
Custom control: Blade's Tip	Number of prism layer: 12 Prism layer Near wall thickness: 6 e-6 m Prism layer total thickness: 0.01%,4 e-4 m
Custom control: Blade	Number of prism layer: 15 Prism layer Near wall thickness: 6 e-6 m Prism layer total thickness: 0.01%,4 e-4 m

Table 5.3: Prism Layer Mesher controls

5.4 Adaptive mesh refinement (AMR)

Once the baseline mesh was defined, an additional mesh refinement step was needed to capture in detail the flow around the blade.

The AMR was used because it refines the computational mesh dynamically only in areas where needed to capture the relevant flow features while recovering coarser cells elsewhere. In order to carry out the refinement, the parameter known as "Q-criterion" was used to identify the vortices coming off the blade [7], [10].

5.4.1 Q-Criterion

According to the study conducted by [11], three different vortices detach and, depending on the operating regime, interact with each other and distort downstream of the propeller. These vortices are called tip vortex, root vortex and hub vortex, named after the point on the propeller where they form.

The Q-criterion is defined as [10]:

$$Q = \frac{1}{2} (\Omega_{ij}\Omega_{ij} - S_{ij}S_{ij}) = \frac{1}{4} (\omega^2 - 2S_{ij}S_{ij}) \quad (5.6)$$

where Ω and S are respectively the antisymmetric and symmetric parts of the velocity gradient tensor.

$$\Omega_{ij} = \frac{1}{2} \left(\frac{\partial u_i}{\partial x_j} - \frac{\partial u_j}{\partial x_i} \right) \quad (5.7)$$

$$S_{ij} = \frac{1}{2} \left(\frac{\partial u_i}{\partial x_j} + \frac{\partial u_j}{\partial x_i} \right) \quad (5.8)$$

The Q-Criterion represents the balance between the vorticity increase Ω^2 and the particle deformation ratio S^2 . In the center of the vortices, the vorticity increases greatly so Q becomes positive.

Assuming incompressibility, we have the following expression:

$$Q = \frac{1}{2} \frac{\nabla^2 p}{\rho}$$

5.4.2 Field Functions Definitions

Having explained the physical meaning of the Q-Criterion, we define a Field Function used for the refinement of the rotating domain and identify the vortex around the blade:

$$\begin{aligned} & ((\$WallDistance > 0.0005) \& \& (\$Qcriterion > 1000)) ? 0.0025 : \\ & \quad ((\$$Position[0] > -0.02) \& \& (\$WallDistance > 0.0005) \& \& \\ & \quad ((pow(\$$Position[1],2) + pow(\$$Position[2],2)) < 0.048)) ? 0.004 : 0 \end{aligned} \quad (5.9)$$

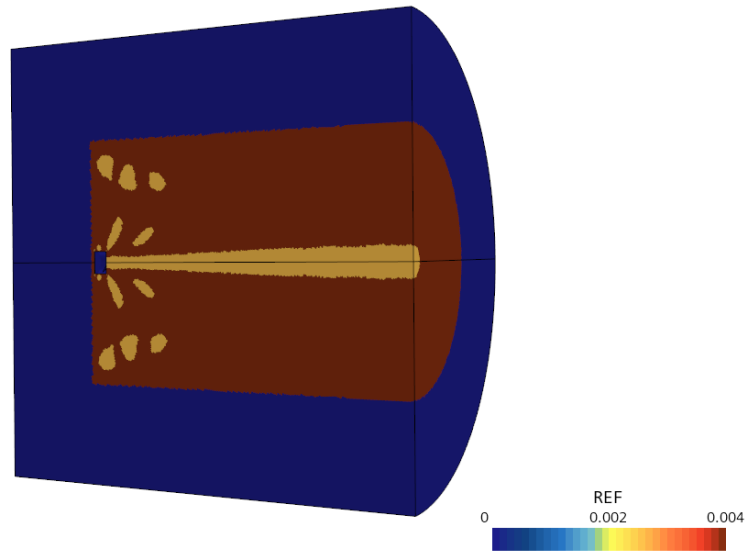


Figure 5.8: Field functions Applications

Figure 5.8 shows how the Q-Criterion can identify vortices and perform a refinement in those regions to resolve them more accurately (yellow region). Through the field function, we also performed a slight refinement of the wake. (brown region).

An example of mesh refinement is shown in the figure below:

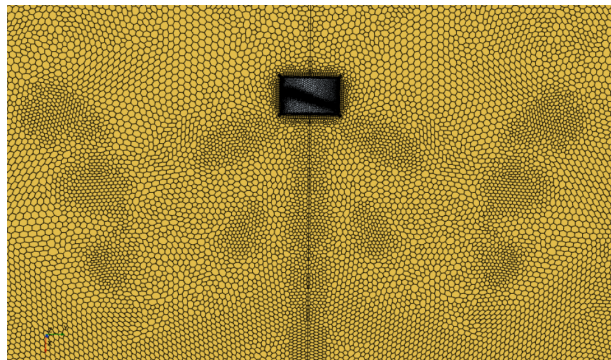


Figure 5.9: Adaptive mesh effect

5.4.3 Refine mesh options

The refinement procedure has been automated and is divided into 3 steps:

- 5000 iterations of baseline mesh to allow the flow to fully develop
- Two adaptive refinement of 2500 iterations plus slight mesh refinement to gradually more accurately capture the three vortices generated by the blade interaction.
- A volumetric refinement in the area contained within the rotating domain will conclude the procedure to convergence

All the parameters assigned to both the mesh during the procedure are given in the following tables:

N°iter:5000	N°iter:5000	N°iter:10000
Base size:4m	3m	3m
D.E: Target Surface Size: 4%,0.16 m Minimum Surface Size: 2%,0.08 m	Target Surface Size: 4%,0.12 m Minimum Surface Size: 2%,0.06 m	Target Surface Size: 4%,0.12 m Minimum Surface Size: 2%,0.06 m
D.R: Target Surface Size: 2%,0.08 m Minimum Surface Size: 1%,0.04 m	Target Surface Size: 2%,0.06 m Minimum Surface Size: 1%,0.03 m	Target Surface Size: 0.15%,4.5e-3 m Minimum Surface Size: 0.1%,3e-3 m Volume Growth Rate: 1.1
Hub: Target Surface Size: 0.5%,0.02 m Minimum Surface Size: 0.05%, 2e-3 m	Target Surface Size: 0.5%,0.015 m Minimum Surface Size: 0.05%, 0.0015 m	Target Surface Size: 0.05%,1.5e-3 m Minimum Surface Size: 0.01%,3e-4 m Volume Growth Rate: 1.1
Tip: Target Surface Size: 0.0075%,3e-4 m Minimum Surface Size: 0.005%,2e-4 m	Target Surface Size: 0.0075%,2.25e-4 m Minimum Surface Size: 0.005%,1.5e-4 m	Target Surface Size: 0.0025%,7.5e-5 m Minimum Surface Size: 0.002%,6e-5 m Volume Growth Rate: 1.1
Blade: Target Surface Size: 0.1%, 4e-3m Minimum Surface Size: 0.01%, 4e-4m	Target Surface Size: 0.1%, 0.003 m Minimum Surface Size: 0.01%, 3e-4m	Target Surface Size: 0.0075%,2.25e-4 m Minimum Surface Size: 0.0025%,7.5e-5 m Volume Growth Rate: 1.1

Table 5.4: Surface refinement

	N°iter:5000	N°iter:10000
Base size	4m	3m
Hub	Number of prism layer:10 Prism layer Near wall thickness:3e-6m Prism layer total thickness:0.01%,4e-4	Number of prism layer:10 Prism layer Near wall thickness:6.2e-6m Prism layer total thickness:0.1%,3e-3
Tip	Number of prism layer:12 Prism layer Near wall thickness:3e-6m Prism layer total thickness:0.01%,4e-4	Number of prism layer:20 Prism layer Near wall thickness:1.2e-6m Prism layer total thickness:0.01%,3e-4
Blade	Number of prism layer:15 Prism layer Near wall thickness:3e-6m Prism layer total thickness:0.01%,4e-4	Number of prism layer:15 Prism layer Near wall thickness:1.2e-6m Prism layer total thickness:0.025%,7.5e-4

Table 5.5: Prism Layer refinement

5.5 Blade P5-D15-S0.1

The analysis procedure, described in the previous sections, was tested on the following geometry. We will use the P5-D15-S0.1 as reference geometry for the comparisons that will be discussed in the next chapter.

It should be mentioned that all the values that will be reported are for a single blade. As we explained in paragraph 5.2, is possible to double them to obtain the values for the complete rotor.

Simcenter STAR-CCM+

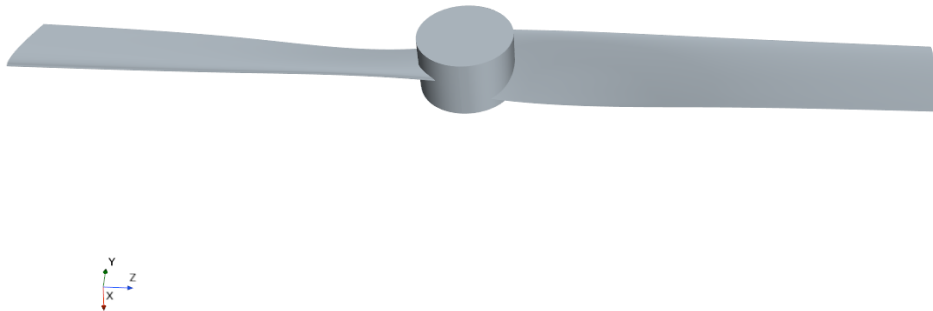


Figure 5.10: Blade P5-D15-S0.1

5.6 Solver Convergence

Three essential conditions must be satisfied to confirm the convergence of the simulation:

- A reduction of the globally scaled residuals by at least 10^{-3} for all equations.
- Stabilization of the residuals quantities for several iterations before stopping the simulations.
- Convergence of integral quantities such as Thrust and Torque

As evident from the figure 5.11, the three phases of mesh refinement can be seen, ending at the 10000 iterations. Additionally, starting from the 19000th iteration, all parameters have exhibited stability, satisfying the initial convergence criterion.

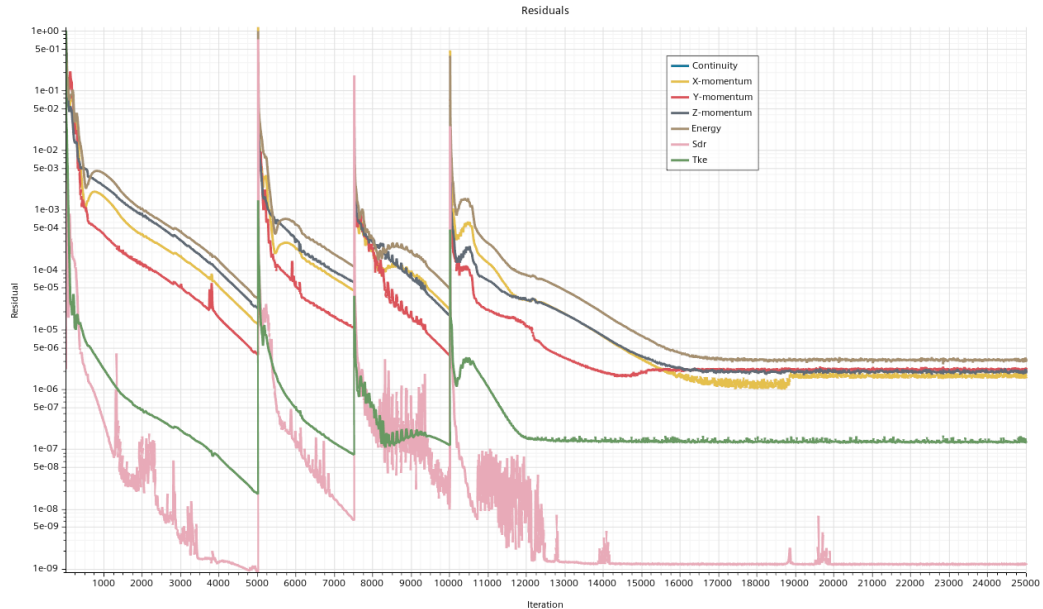


Figure 5.11: Residuals convergence

The same assessment was carried out for the aerodynamic parameters under study as introduced in Chapter 2.

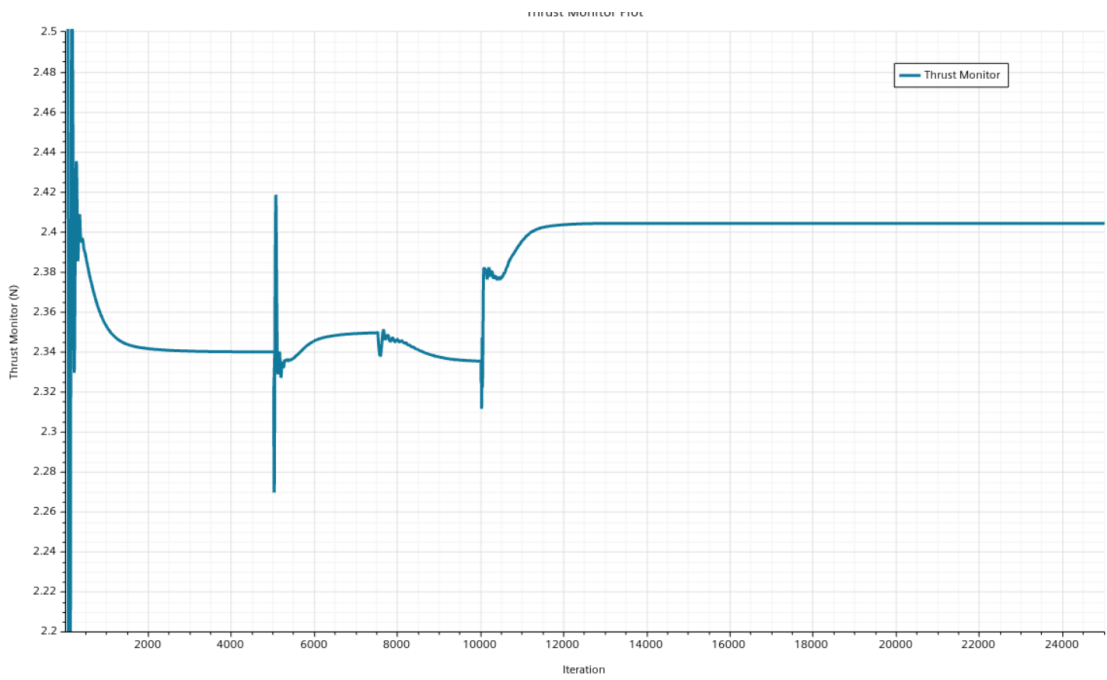


Figure 5.12: Thrust convergence

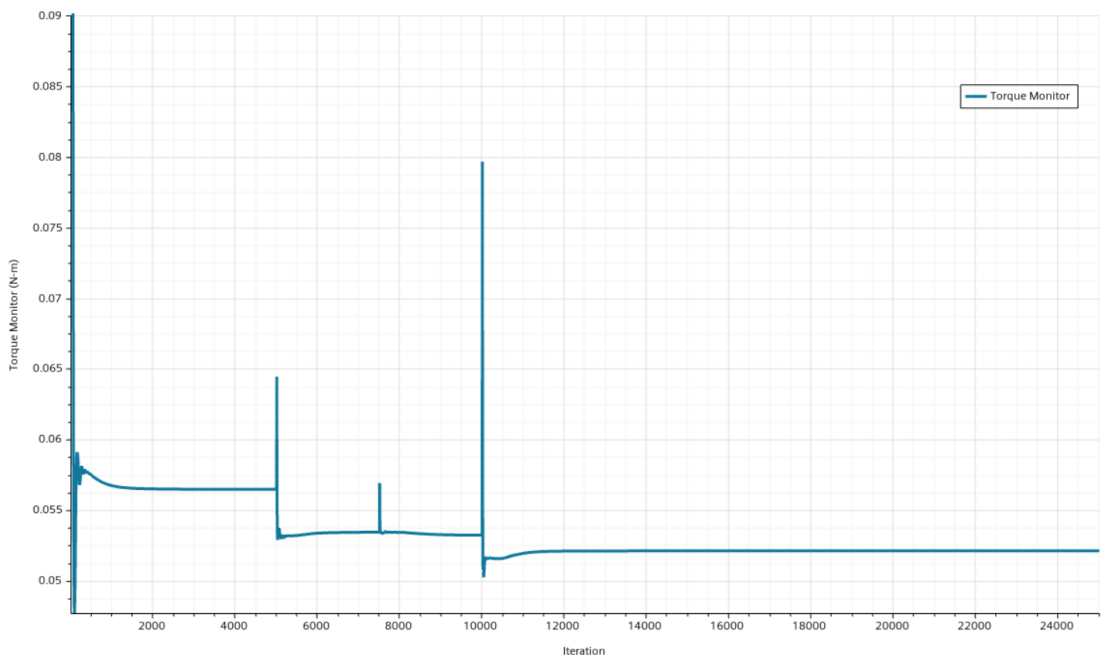


Figure 5.13: Torque convergence

5.7 Performance Analysis

The obtained aerodynamic parameter values, in 5.6, will be used to evaluate the impact of the geometric changes.

Thrust	Torque	C_T	C_Q	FM
2.404 [N]	0.0521 [N*m]	0.0101	0.0011	0.63

Table 5.6: Performance value of P5-D15-S0.1

Given that in the hovering condition, the definitions of efficiency and feed ratio are meaningless due to zero velocity, we evaluated the efficiency (figure of merit) using the following equation [2]:

$$FM = \frac{1}{\sqrt{2\rho}} \frac{T}{P} \sqrt{\frac{T}{A}} \quad (5.10)$$

According to [2], a rotor with good performance in hovering is characterized by $FM \approx 0.7/0.8$.

In addition, the distribution of these quantities along the blade geometry was also evaluated. These graphs will provide valuable insights into how performance varies locally with changes in geometry.

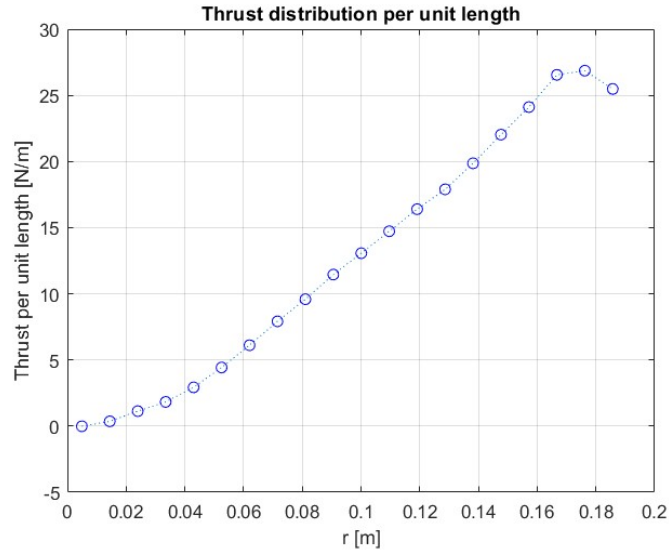


Figure 5.14: Thrust distribution per unit length

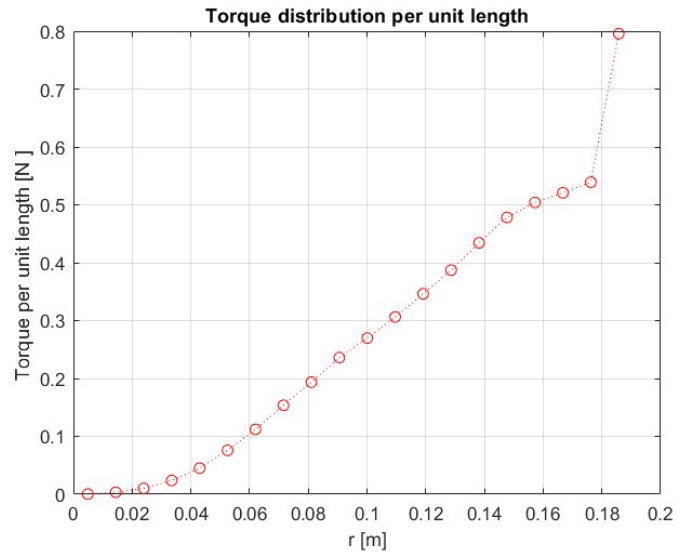


Figure 5.15: Torque distribution per unit length

The trends obtained are quite accurate, comparing them with the one reported in [12], especially up to 80-90%. Towards the blade’s end, the curves exhibit a slightly modified pattern, particularly evident in the torque graph which could be caused by the effect of the tip vortex.

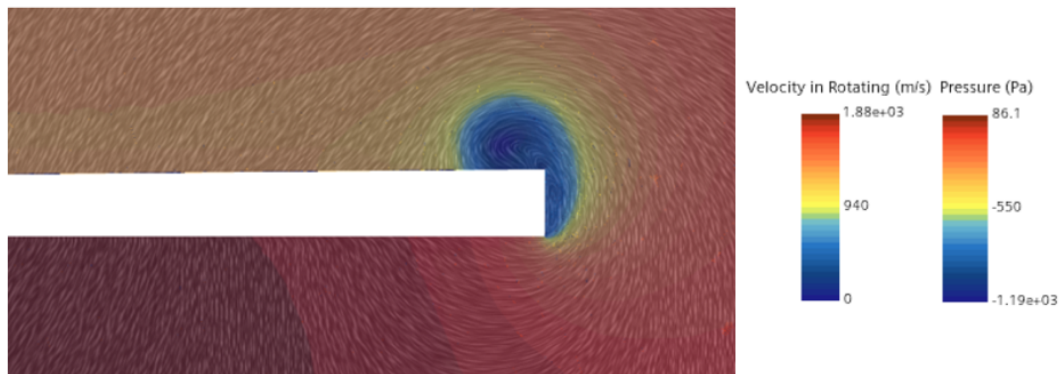


Figure 5.16: Tip vortex visualization

As depicted in Figure 5.16, the tip vortex is formed when high-pressure air under the wing flows outward and meets with low-pressure air above the wing. This pressure differential gives rise to a force encircling the wingtip, consequently shaping the vortex. The existence of the vortex tip at the blade’s end leads to an augmentation

of the local velocity at the tip, subsequently causing a decrease in pressure, as illustrated in figure 5.16.

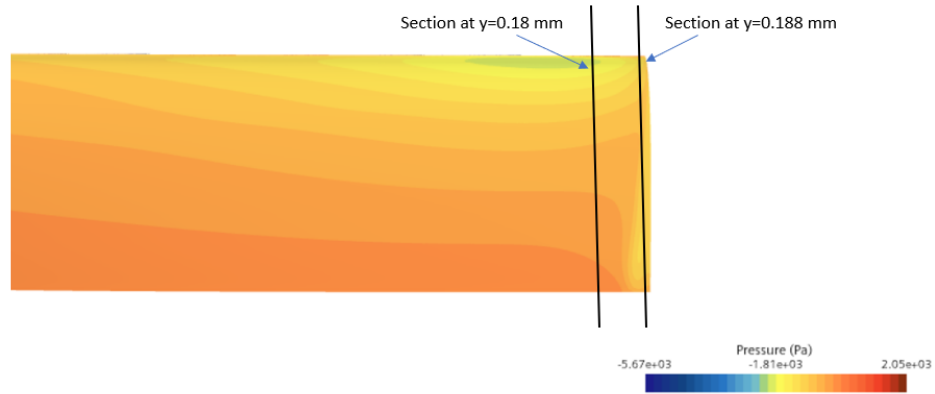


Figure 5.17: Low-pressure zone at the tip of the blade

The decrease in pressure induced by the vortex at the tip leads to a suction peak. In order to see this peak we assessed the pressure distribution in the two areas highlighted in figure 5.17.

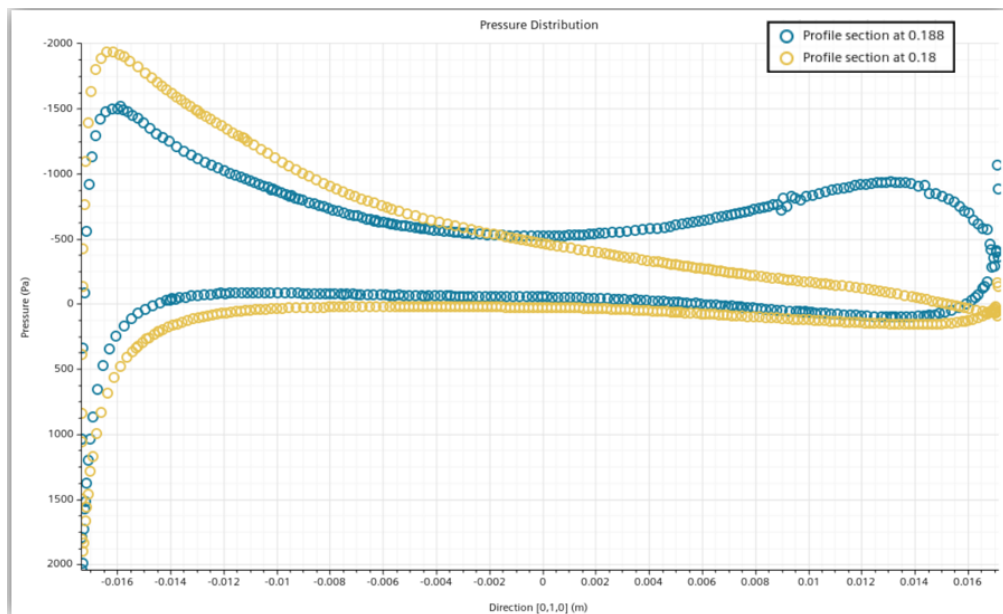


Figure 5.18: Comparison of pressure distribution in two blade sections

Through the figure 5.18, we can clearly see the suction peak which is not present in the other section. Furthermore, owing to this suction peak, the pressure distribution covers a larger area compared to one of the other sections, resulting in an increase in the generated Lift. However, this marginal Lift increase is offset by a substantial rise in induced Drag, primarily responsible for the spike highlighted in graph 5.15.

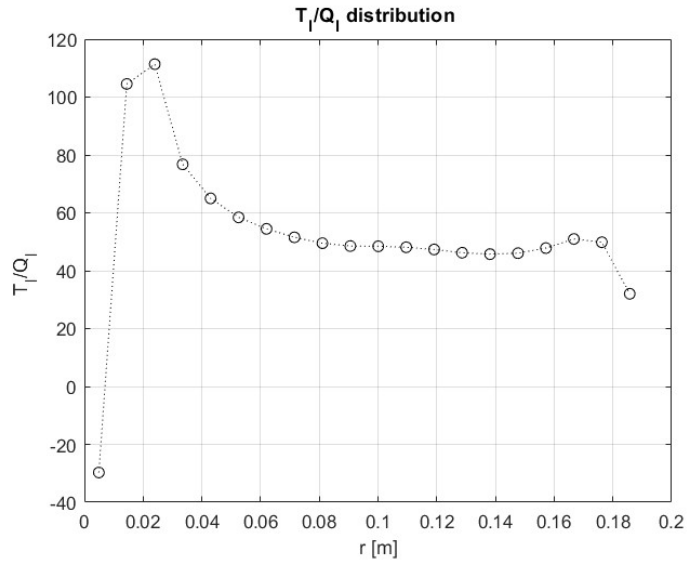


Figure 5.19: T/Q distribution per unit length

Furthermore, figure 5.19 shows the disadvantage of this vortex structure with the need to introduce a tip correction to mitigate the tip vortex effect.

5.8 Qualitative data

Since these vortex structures influence the blade's performance, it is interesting to evaluate potential shape, position, and size alterations with variations in the key geometric parameters. As reported in [11], three wake vortices develop in a helix: a hub vortex, a root vortex, and the one starting from the ends of the blade, known as a tip vortex.

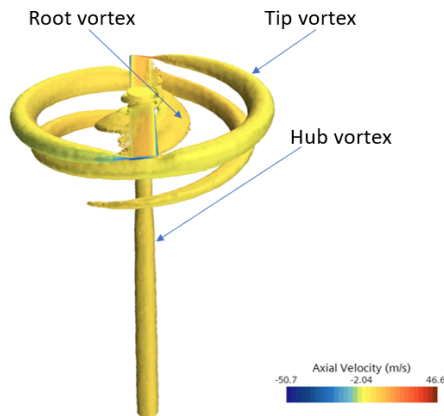


Figure 5.20: Isosurface Q-Criterion $5000/s^2$

In order to notice possible changes during the geometry comparison some analysis of different Q-Criterion sections will be performed:

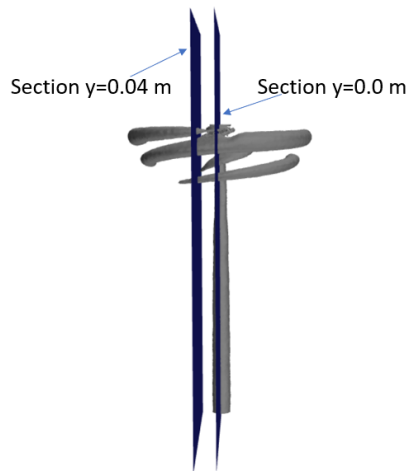


Figure 5.21: Q-criterion Y-section at 0.00 m and 0.04 m

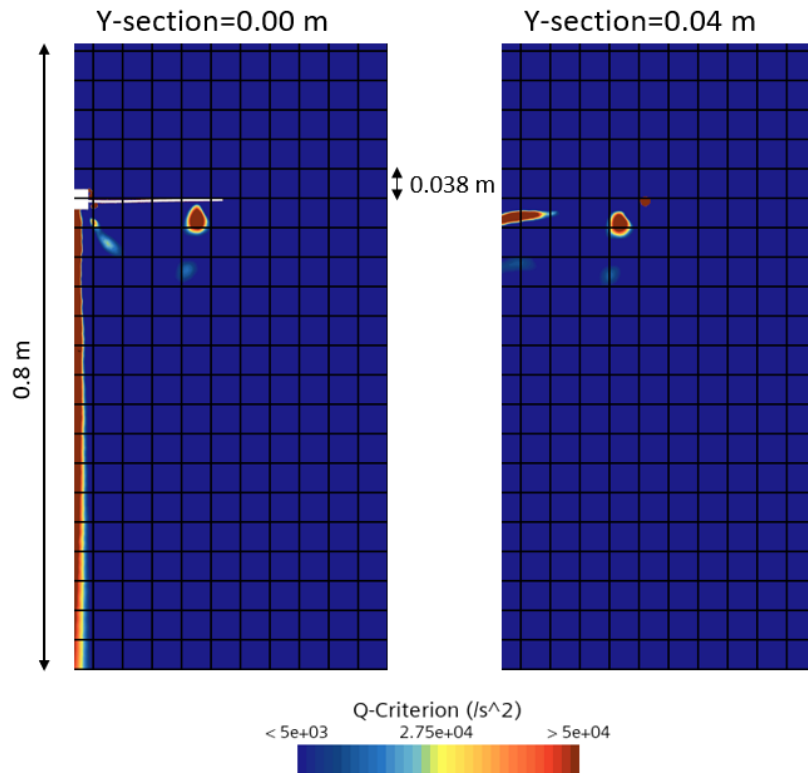


Figure 5.22: Q-criterion Y-section

Through this section, all three vortex structures can be identified. Near the end of the blade, we can see the tip vortex which has already made a half rotation around the blade and passed underneath it. Slightly further down it is possible to notice the same vortex, which accomplished another rotation, reduced its size and it is less intense. These details are a symptom of the dissipation of the vortex. Near the hub of the blade, an important vortex is clearly visible, which is generated downstream of the blade. Lastly, we can identify the root vortex that has a very thin structure with two zones of peak Q-criterion.

The section at $y=0.04$ m provides a detailed view of the vortex forming at the wing tip and its complete evolution. The vortex, visible in the upper right corner, is gaining energy, leading to an increase in its size in the first rotation. After that, it gradually decreases his peak of the Q-criterion, indicating a reduction in vorticity. Furthermore, this image showcases the fully developed vortex at the wing's root, displaying its distinctive characteristic shape.

To conclude the qualitative study made on our geometry, the "Wall Shear Stress" parameter was evaluated. With this quantity, it is possible to identify the areas of main flow separation leading to the formation of the previously analyzed vortices. In fact, negative values of this quantity denote flow separations.

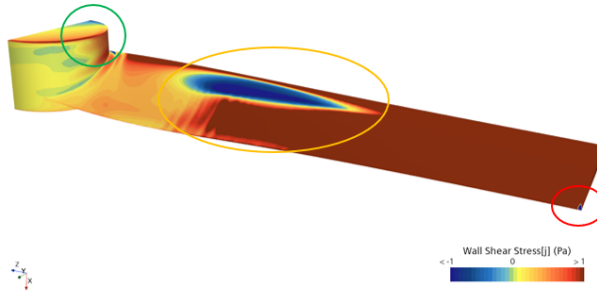


Figure 5.23: Wall Shear Stress

In figure 5.23, several areas where the Wall Shear Stress is negative are highlighted. The first one, the red circle, highlights a little separation point at the tip of the blade. The orange one highlights a huge separation zone on the upper surface of the blade. We can identify both the "line of separation" and the "line of reattachment". Its extension is comparable to the root vortex dimensions visible in figure 5.22. Lastly, the green one highlights the separation area on the blade's hub.

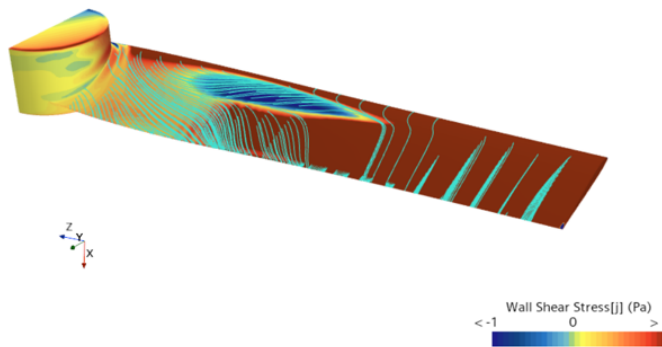


Figure 5.24: Cell Relative Velocity streamlines on the blade with separation detail

Figure 5.24, shows the relative velocity of the cells between the blades. The flow in the positive "Wall Shear Stress" zone remains attached to the blade and follows its shape. In contrast, in the separation zone, the flow tends to move radially toward the blade tip under the influence of centrifugal force and subsequently aligns with the blade's shape at the reattachment line.

Lastly, with figure 5.25, we can observe a region characterized by negative velocity near the wingtip, where the counter-rotating vortices are located.

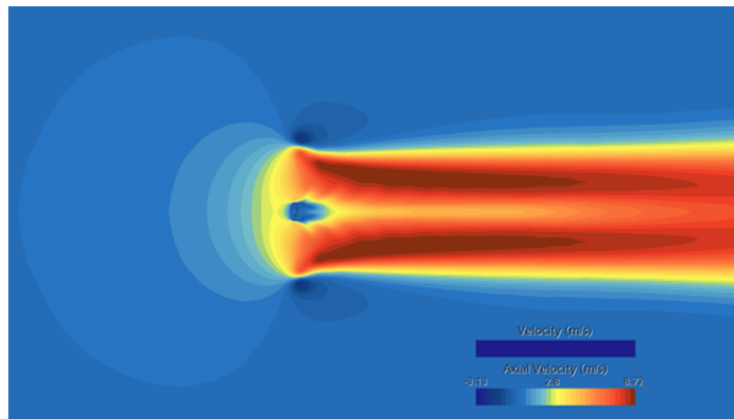


Figure 5.25: Detail of the downstream wake

5.9 Mesh independence study

To conclude the study of blade **p5-d15-s0.1**, an analysis of the effect of mesh was carried out. The following configurations were obtained by modifying the base size from the baseline.

The cases analyzed are reported below:

Cells [Millions]	Base size	Thrust [N]	Torque [N*m]
1	Baseline Mesh	2.34	0.054
3	6m	2.3828	0.0522
6	4m	2.412	0.052
9	3m	2.404	0.0521
20	2m	2.43	0.0523

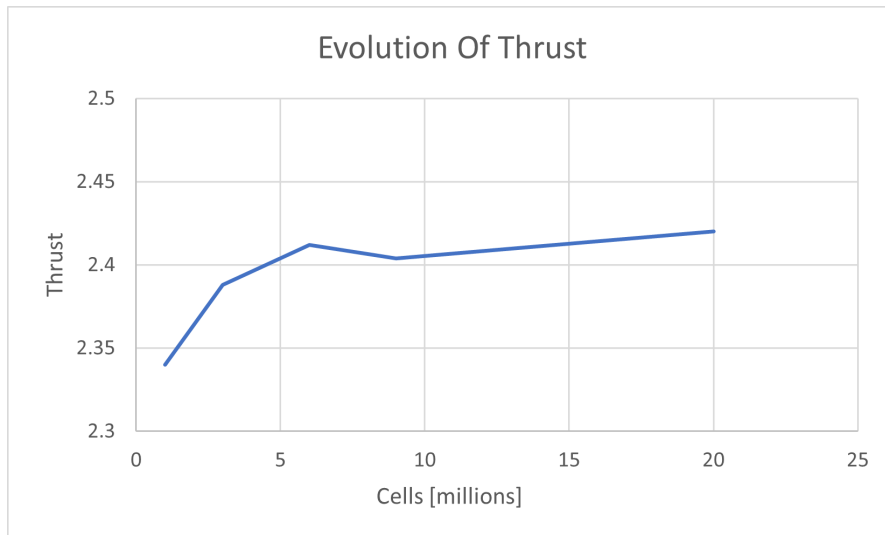


Figure 5.26: Effect of mesh variations on the Thrust

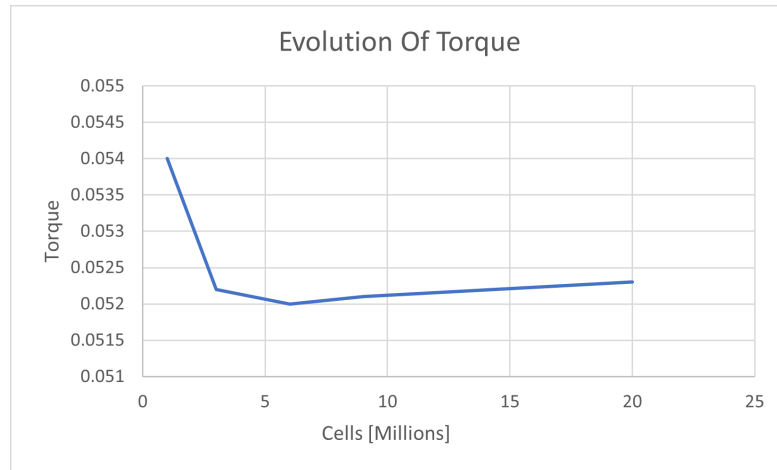


Figure 5.27: Effect of mesh variations on the Torque

For both the aerodynamic parameters, the effect of variation from one mesh to another after 6 million doesn't even reach one percent. This result shows the crucial role of adaptive refinement since, once the vortical structures have been solved, an increase in the mesh has a low impact on the solution.

Subsequently, we evaluated local variations by plotting the distribution of Thrust and Torque as the mesh was modified.

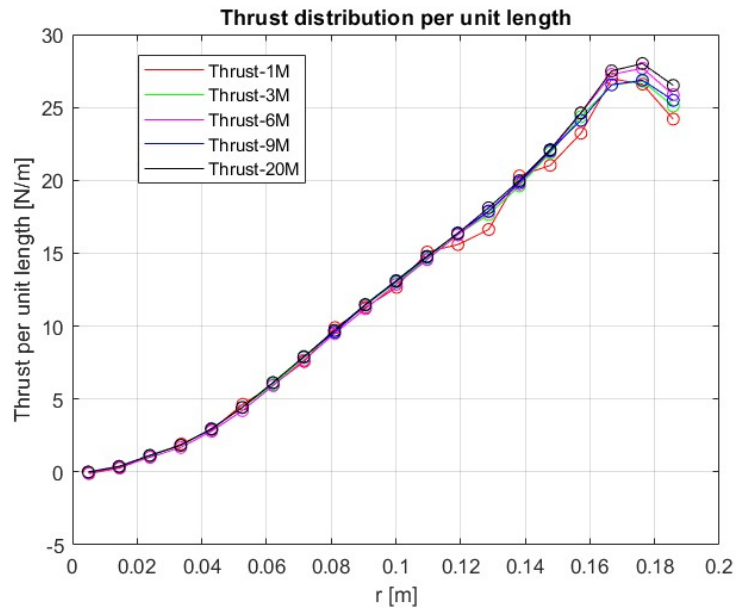


Figure 5.28: Effect of mesh on Thrust distribution

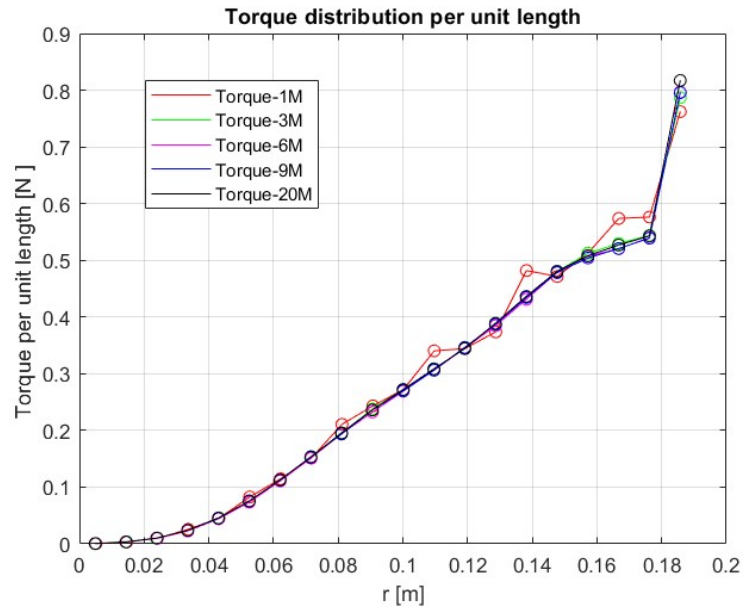


Figure 5.29: Effect of mesh on Torque distribution

In the following graphs, it is evident that local variations are noticeable only in the case with 1 million cells, where the mesh remains relatively coarse. Conversely, in the other cases, there is minimal variation observed across the various simulations.

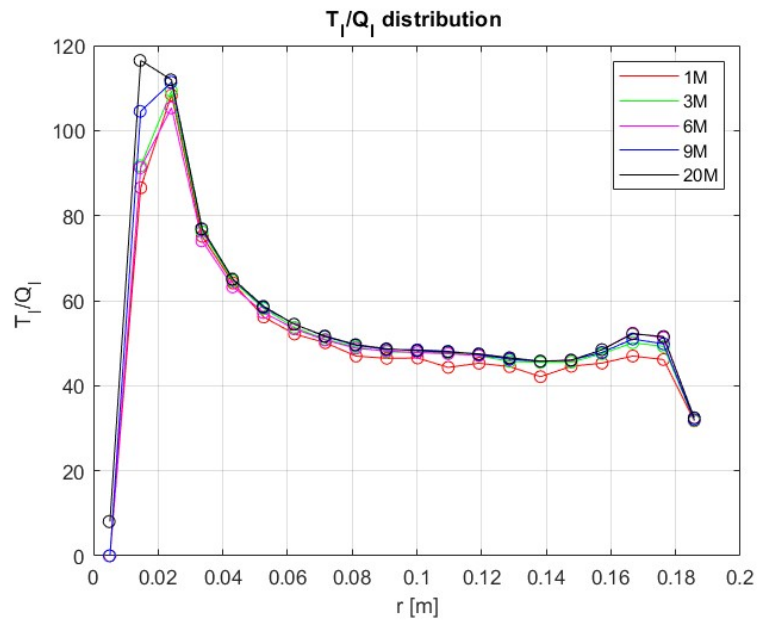


Figure 5.30: Effect of mesh on T/Q distribution

Chapter 6

Effects of geometric variations on blade performance

After concluding the validation of the analysis procedure and the description of the target geometry, in this chapter, we will investigate the effects of geometric variations on blade performance and possible changes in the vortical structures.

The simulations that were carried out are:

- 2 analyses to evaluate the effect of solidity variation
- 2 analyses to evaluate the effect of pitch variation
- 2 analysis to evaluate the effect of the variation of the chord distribution

6.1 Effect of the solidity

The geometries tested to study the effect of this parameter are:

- Blade p5-d15-**Solidity 0.05**
- Blade p5-d15-**Solidity 0.1**
- Blade p5-d15-**Solidity 0.15**

The selection of these solidity values stems from the common rotor solidity ratios observed in helicopters, which generally fall within the range of 0.05 to 0.12. For these tests, the pitch and diameter were fixed to 5 and 15 respectively.

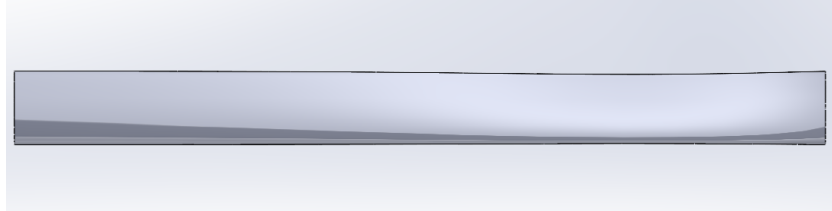


Figure 6.1: Blade-solidity 0.05

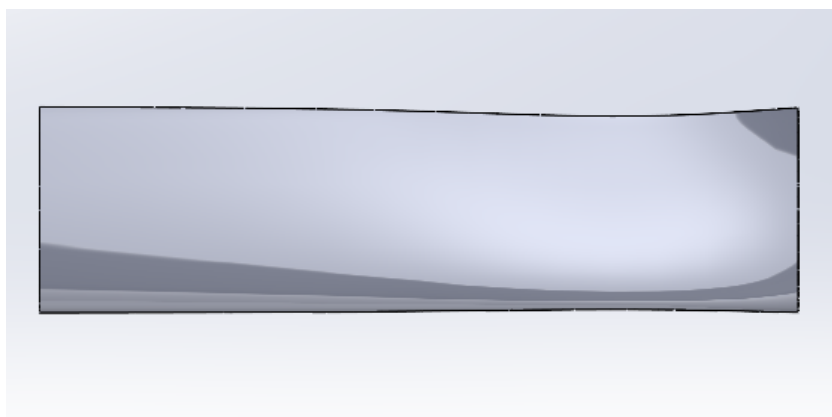


Figure 6.2: Blade-solidity 0.15

6.1.1 Comparison of aerodynamic parameters

The average results obtained for the three blades under analysis are reported in the table below:

Geometry	Average Thrust[N]	Average Torque[N*m]	% variation Thrust	% variation Torque
Blade_p5_ d15-s0.05	1.485	0.0295	-38.2%	-43,4%
Blade_p5_ d15-s0.1	2.404	0.0521	-----	-----
Blade_p5_ d15-s0.15	2.983	0.0728	24%	39.7%

Table 6.1: Performance change with solidity (baseline in yellow)

First of all, we can see that the growth of solidity translates into an increase in the two parameters. Moreover, the percentage variation in Torque is approximately linear, while Thrust variations are more irregular.

The non-linear variation of the Thrust can be explained using the following equation:

$$T = N \int_0^R \left[\frac{1}{2} \rho V_E^2 c C_l \cos(\phi + \alpha_i) \right] dr$$

In fact, considering the equations 3.1 and 3.2, it can be seen that a change in solidity results in a change in chord length which means that Thrust will change. The growth of Thrust implies that induced speed will also increase with a consequent reduction in α_i . This reduction subsequently dampens the growth of Thrust, causing the observed non-linearity.

In order to evaluate the Efficiency of the geometry, we determined the Power required by each geometric configuration to generate the same Thrust of the target, as follows:

- Calculation of rotational speed for the same Thrust

$$\Omega_n = \Omega_t \sqrt{\frac{T_t}{T_n}}$$

- Calculation of Torque for the same Thrust

$$Q_t = Q_n \sqrt{\frac{T_t}{T_n}}$$

- Calculation of the Power required

$$P_t = Q_t \Omega_t$$

Geometry	Average Thrust[N]	Ω [RPM]	Power [W]	% variation Power
Blade_p5_d 15-s0.05	2.404	3817	19.09	16,6%
Blade_p5_d 15-s0.1	2.404	3000	16.37	-----
Blade_p5_d 15-s0.15	2.404	2693	16.55	1,1%

Table 6.2: Change in Power required with solidity

From the result obtained, we can say that there will be a configuration of optimum between 0.1 and 0.15.

In addition, a study of local variations in aerodynamic forces was carried out to see where the effect of solidity predominates.

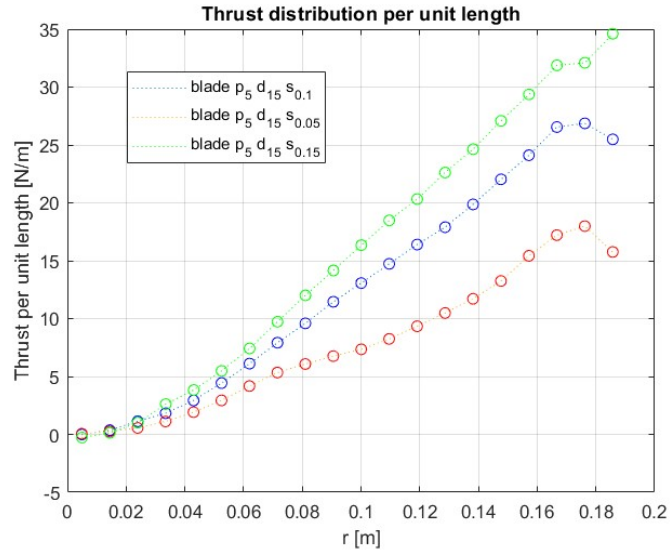


Figure 6.3: Change of Thrust distribution with solidity

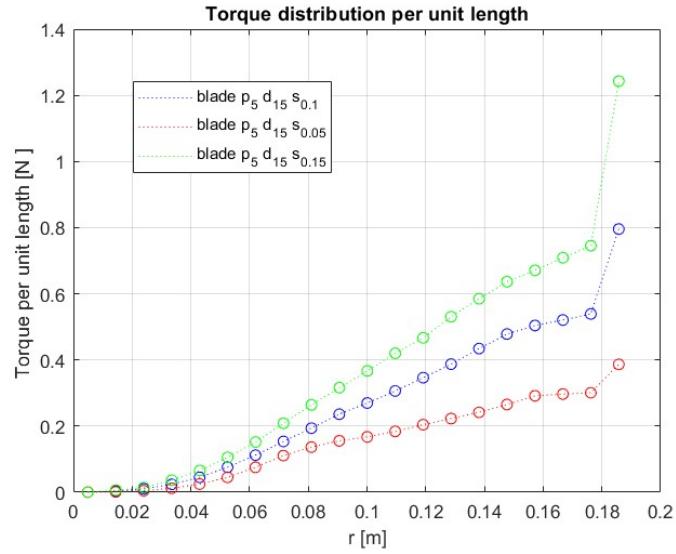


Figure 6.4: Change of Torque distribution with solidity

It is noticeable that the trend of the Thrust and Torque distribution curves maintains the typical behavior observed in [12]. In the first 25% of the blade, the distributions are almost identical, with minimal variations. The effect of solidity variation gradually becomes visible as we move toward the tip, which is likely due to the tip vortex effect.

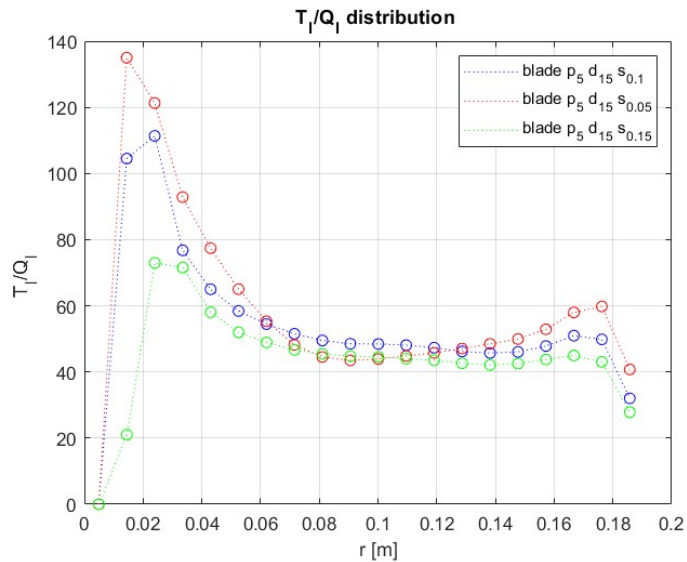


Figure 6.5: Change in T/Q distribution with solidity

6.1.2 Qualitative Data

To conclude the study of this parameter, it is also interesting to evaluate how the vortical structures changed through a Q-Criterion isosurface scene:

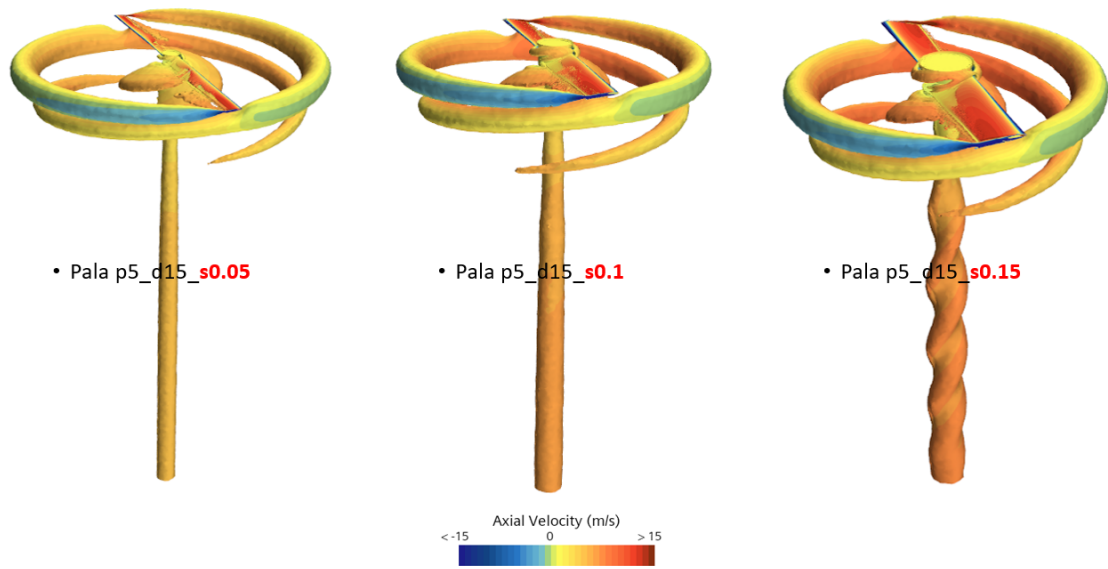


Figure 6.6: Comparison vortex structure Isosurface $Q=5000/s^2$

In the figure 6.6, we can notice a difference in the size of the hub vortex. This growth is primarily caused by the augmented blade chord size. Furthermore, it is evident that the vortex structure's shape at the hub is different from the one of the target. This disparity is likely attributed to an interaction with the root vortex. Lastly, the tip vortex seems to enlarge as solidity increases, but quantifying the exact growth is challenging in this scene.

In order to have a more accurate view of changes in the vortex structures, the Q-Criterion parameter was evaluated at different Y-sections.

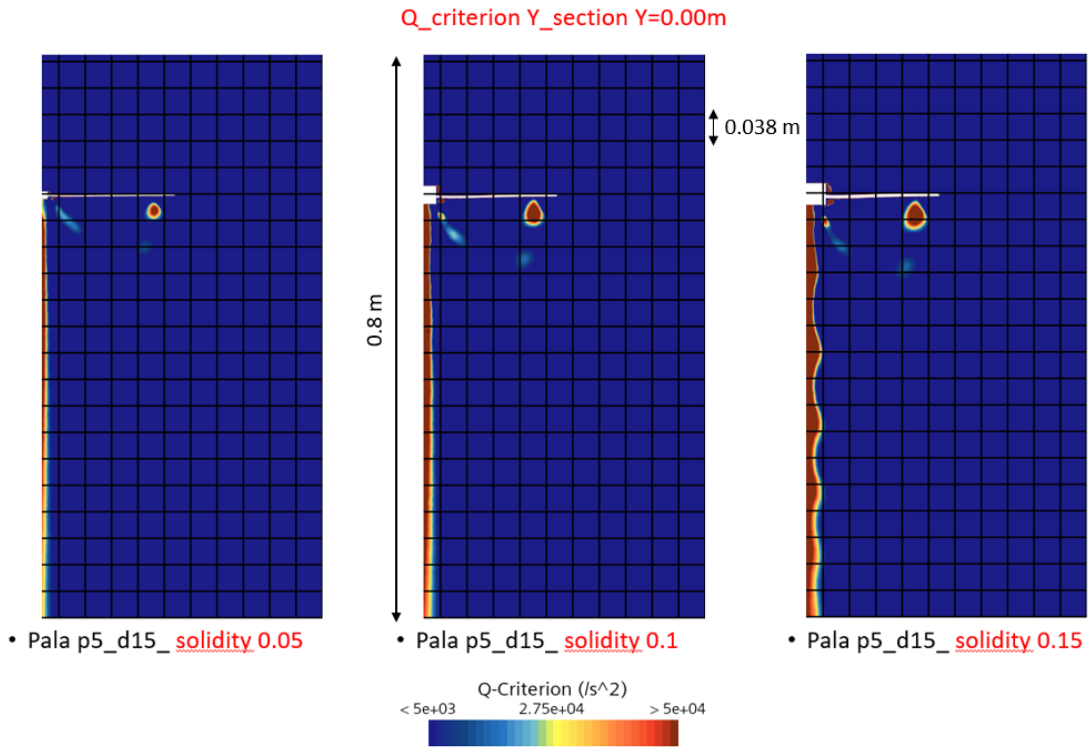


Figure 6.7: Comparison vortex structure $Y=0.0$ m

Near the blade tip, we can observe a vortex after completing a half rotation around the blade. The increasing solidity leads to a larger vortex, reaching up to 4 cm in extreme cases. The zone of high vorticity also tends to expand with the growth of the chord. The proximity to the blade's lower surface causes a change in the vortex shape which assumes a conical form instead of the one that can be observed in the left figure. Lastly, at the blade root, the increase in solidity resulted in a vortex shift along with the formation of a vorticity peak.

The next figure, instead, is presented to analyze the vortices immediately after they have formed.

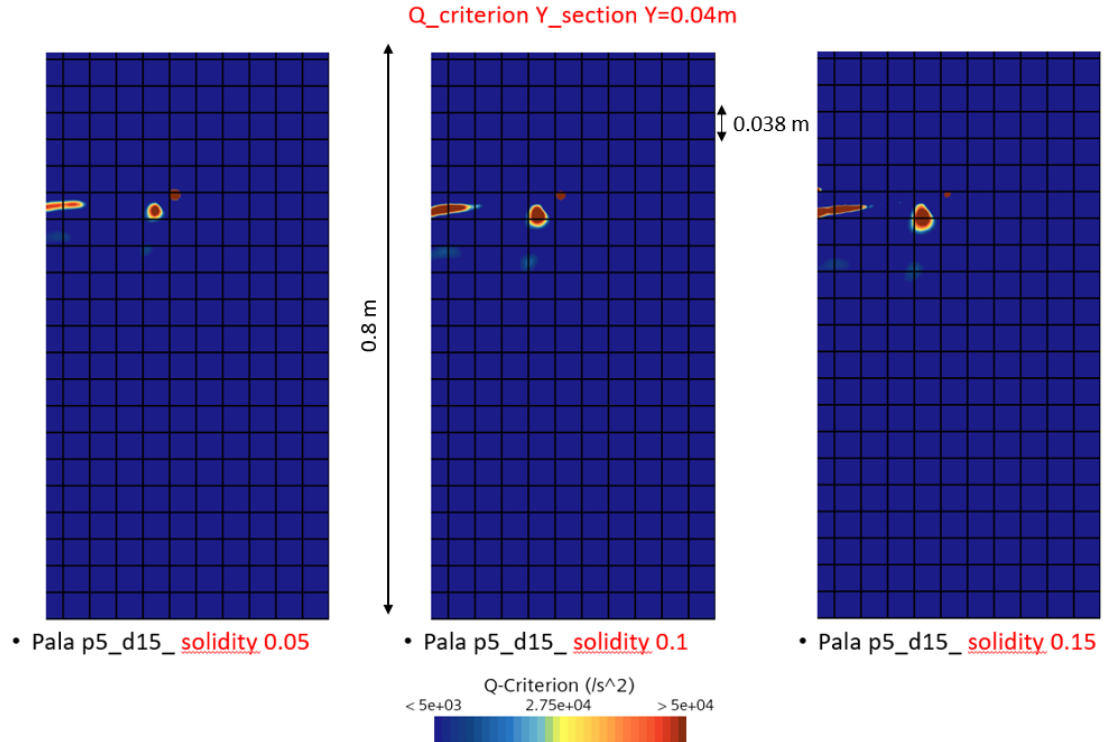


Figure 6.8: Comparison vortex structure $Y=0.04$ m

The tip vortex on the the left figure gains energy more rapidly, resulting in a faster increase in size compared to the other configurations, but it tends to dissipate quicker as we have seen in 6.7.

Moreover, this section allows us to see some changes in the root vortex structure. The blade, with a solidity equal to 0.15, exhibits a narrower and more extensive vortex probably caused by a slightly larger separation zone compared to the target geometry.

6.2 Effect of the pitch

The geometries tested to study the effect of this parameter are:

- Blade pitch5-d15-s0.1
- Blade pitch7-d15-s0.1
- Blade pitch10-d15-s0.1

The choice of these configurations was made to gradually evaluate the change in the pitch parameter. In these cases, the solidity and diameter were fixed.

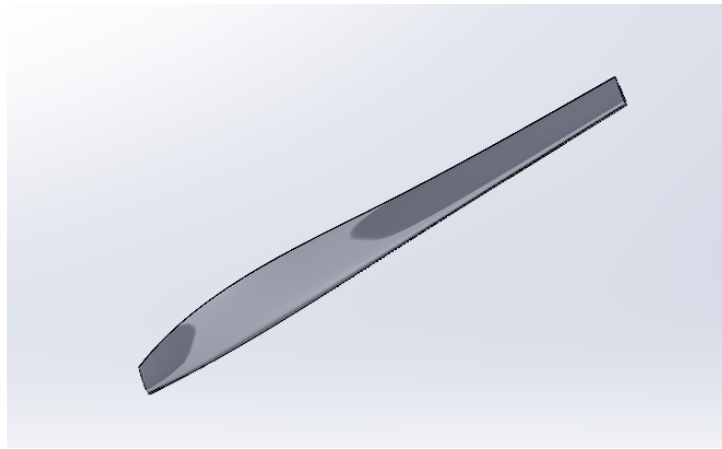


Figure 6.9: Blade-pitch 7

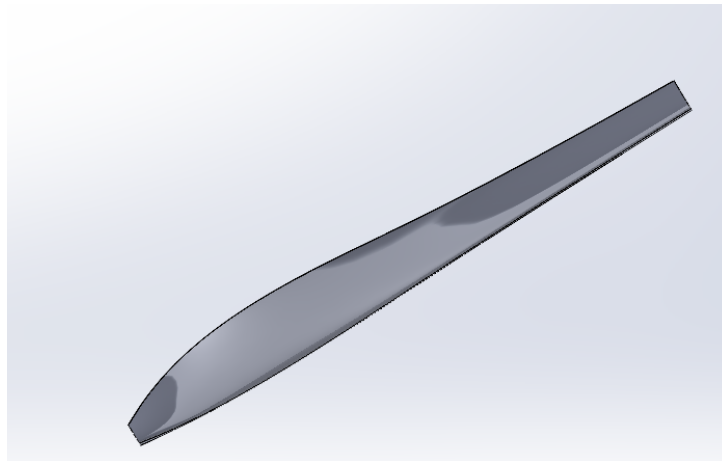


Figure 6.10: Blade-pitch 10

6.2.1 Comparison of aerodynamic parameters

The average results obtained for the three blades under analysis are reported in the table below:

Geometry	Average Thrust[N]	Average Torque[N*m]	% variation Thrust	% variation Torque
Blade_p5_d15-s0.1	2.404	0.0521	-----	-----
Blade_p7_d15-s0.1	3.428	0.0895	42,6%	71,9%
Blade_p10_d15-s0.1	4.301	0.1902	78,9%	265,1%

Table 6.3: Performance change with pitch angle (baseline in yellow)

The data underlines a notable influence of pitch variation on the rotor blade's Thrust and Torque. The Thrust demonstrated an almost linear increase with the parameter while the Torque showed a sharper growth, reaching an impressive 265% increase compared to the target one.

The growth in aerodynamic parameters is obviously evident since, considering the equations 3.3 and 2.25, a change in pitch results in the growth of the angle of attack on each section of the airfoil. As a result, there will be an increase in Lift, subsequently leading to an increase in Thrust and Torque.

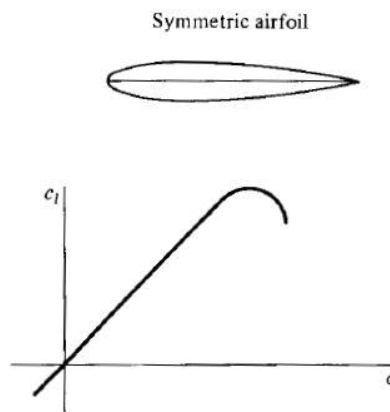


Figure 6.11: CL vs alpha

Although the variation of pitch guaranteed a significant rise in the Thrust, the sharp spike in Torque growth underscores the necessity of conducting a study on the required Power. This analysis aims to find out if there will be an improvement compared to the target configuration.

Geometry	Average Thrust[N]	Ω [RPM]	Power [W]	% variation Power
Blade_p5_d15-s0.1	2.404	3000	16.37	-----
Blade_p7_d15-s0.1	2.404	2512	16.51	0,9%
Blade_p10_d15-s0.1	2.404	2243	24.97	52,5%

Table 6.4: Change in Power required with pitch

The high Power required for the high-pitch configuration suggests that the blade is probably near stall and is disadvantageous to be used compared to the baseline configuration.

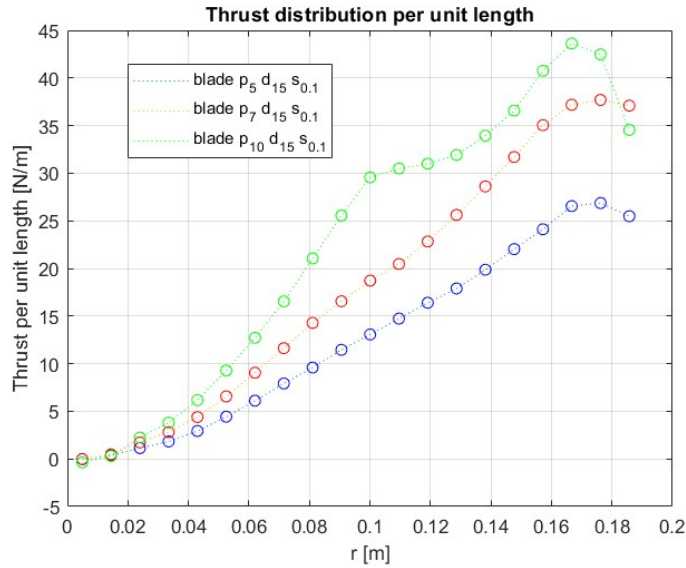


Figure 6.12: Change of thrust distribution with pitch

In terms of local distribution, the Blade pitch7-d15-s0.1 maintains a similar trend to the baseline one, with a slight local increase as we approach the blade end.

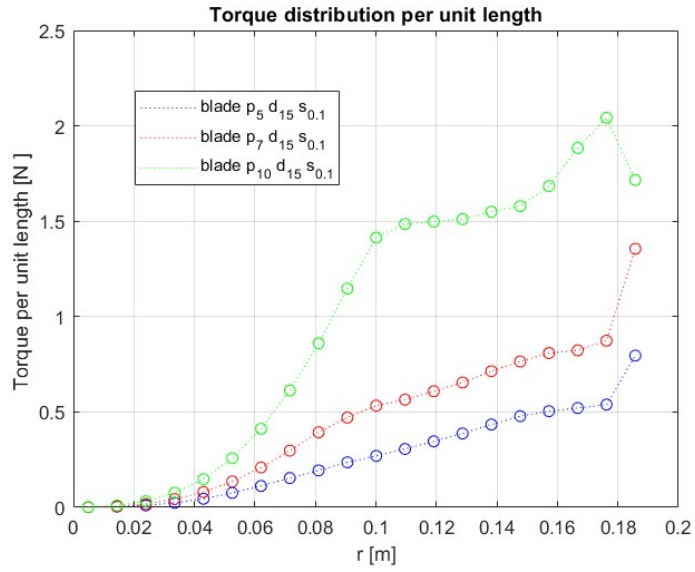


Figure 6.13: Change of torque distribution with pitch

The high-pitch blade has an altered Thrust and Torque distribution compared to the baseline. In detail, it can be seen that the Thrust and Torque tend to increase in the first half of the blade reaching a peak. Afterward, there is a plateau in growth, followed by an increase in the last section of the blade with a varying slope.

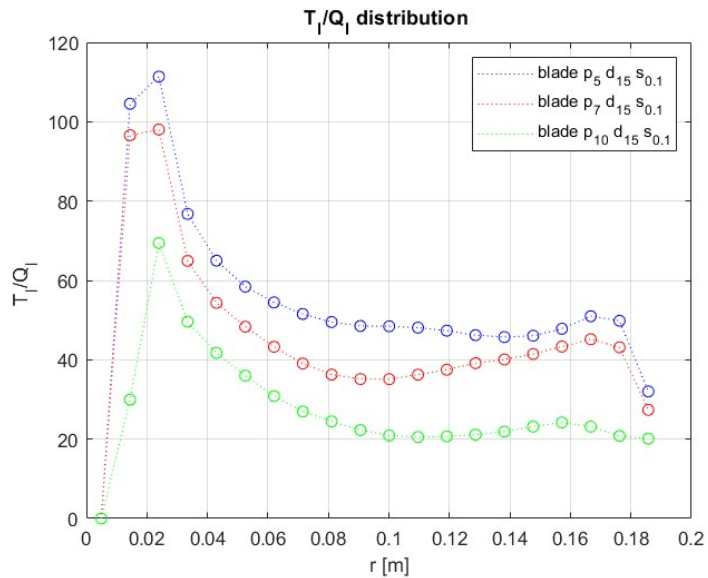


Figure 6.14: Change in T/Q distribution with pitch

Observing the graph below, the plateau observed near the blade's tip in the high-pitch configuration indicates a likely separation zone. Based on the previous observation, it has been decided to also evaluate the "Wall Shear Stress" parameter to assess any potential changes in the central separation zone identified in the target configuration.

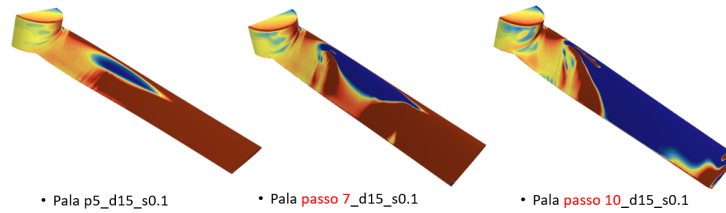


Figure 6.15: Difference region of separation

The figure shows the separation region on our blade. In the intermediate one, the region is still small and does not extend throughout the entire length of the blade. On the other hand, the Blade pitch10-d15-s0.1 shows a region that is almost extended for the entire upper surface. This extended separation zone is the cause of the high power required shown in table 6.4.

6.2.2 Qualitative Data

Since the significant increase in aerodynamic parameters and the change in the separation zone, it is also interesting to evaluate how the vortex structures have changed.

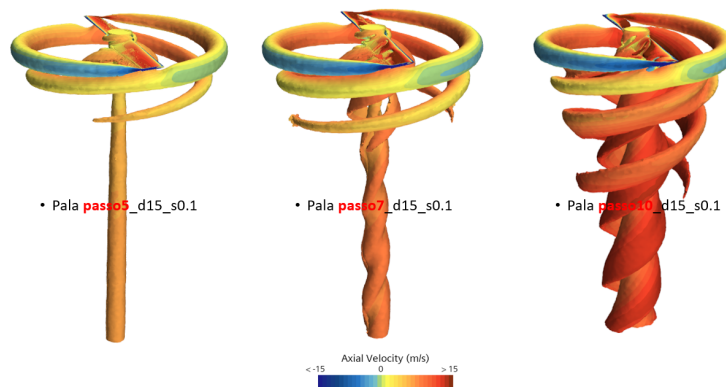


Figure 6.16: Comparison vortex structure $Q=5000/s^2$

The visualization of the iso-surfaces of Q-Criterion allows us to make a first comparison between the vortex structures. The geometry, with an intermediate pitch value, has visible differences in the dimensions of both the vortex that detaches from the hub and the tip. The root vortex seems also more extended and probably interacts with the hub vortex.

As for the geometry with the greatest variation in pitch, it showcases intricate and disorderly vortex structures that diverge from the baseline one. Although the RANS method cannot predict with high accuracy the separation zone for the high-pitch blade, potentially leading to disparities between the depicted vortex structures and actual phenomena, we decided to analyze the acquired geometry to elucidate the observed differences in Power required.

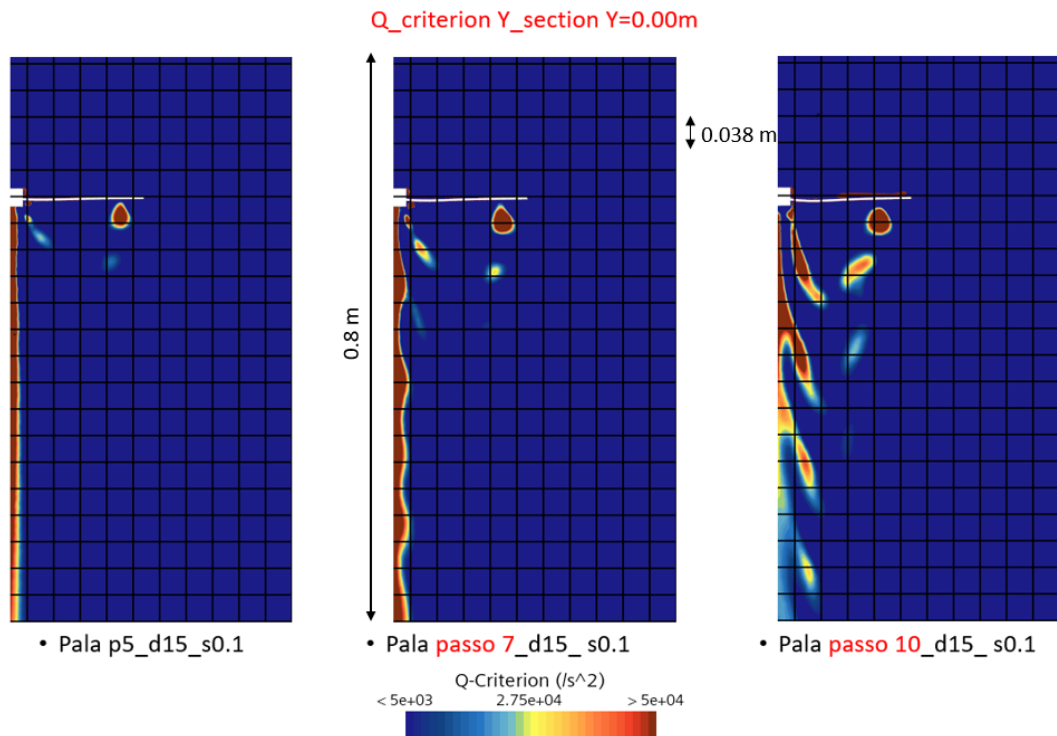


Figure 6.17: Comparison vortex structure $Y=0.0$ m

Comparing the first two geometries, it is noticeable how the pitch increase leads to an overall expansion of the areas of all three vortex structures.

The high-pitch geometry, instead, shows evident changes. First of all, a more extended and rounded tip vortex is observed. This vortex, after completing the second revolution around the structure, interacts with the separation flow modifying its shape.

The root vortex also exhibits significant differences and appears considerably stretched out. It also interacts with the hub vortex after completing the second revolution, modifying the shape of the hub one.

6.3 Effect of the cord distribution change

The geometries tested to study the effect of this parameter are:

- Blade p5-d15-s0.1 with fixed chord
- Blade p5-d15-s0.1 with chord peak at 50%
- Blade p5-d15-s0.1 with chord peak at 25%

The choice of these two configurations was explained in 3.3:

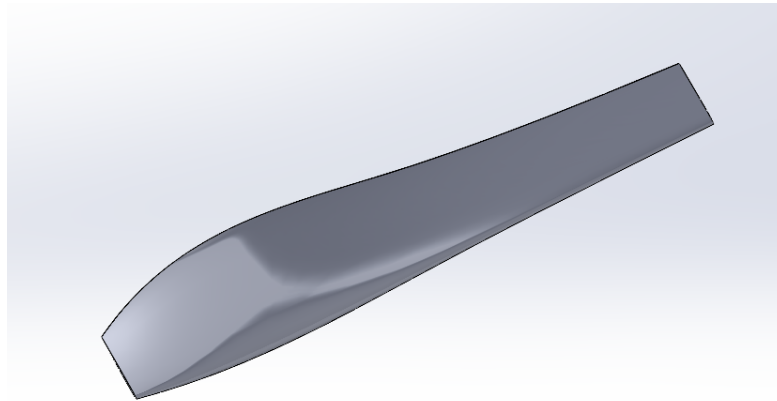


Figure 6.18: Blade p5-d15-s0.1 with chord peak near the 25%

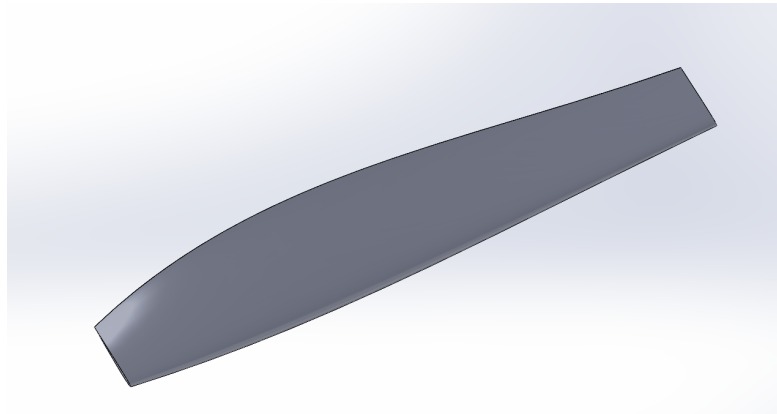


Figure 6.19: Blade p5-d15-s0.1 with chord peak near the 50%

6.3.1 Comparison of aerodynamic parameters

The average results obtained for the three blades are shown in the table below:

Geometry	Average Thrust[N]	Average Torque[N*m]	% variation Thrust	% variation Torque
Blade_p5_d15-s0.1	2.404	0.0521	-----	-----
Blade_p5_d15-s0.1 peak25%	2.163	0.0439	-10,0%	-15,7%
Blade_p5_d15-s0.1 peak50%	2.020	0.0412	-16,0%	-20,9%

Table 6.5: Performance change with changing in the chord distribution

The results show that the chord variation has a significantly lower effect on the parameters compared to the others examined. In the two configurations, there is a decrease in both Thrust and Torque less than 20% compared to the baseline configuration. This result is due to the displacement of the chord to the root of the blade which is a less efficient area in generating Thrust and Torque.

As these configurations are primarily focused on improving Efficiency, we calculated the required Power to assess whether there was any improvement compared to the target geometry.

Geometry	Average Thrust[N]	Ω [RPM]	Power [W]	% variation Power
Blade_p5_d15-s0.1	2.404	3000	16.37	-----
Blade_p5_d15-s0.1 peak25%	2.404	3163	16.16	-1,3%
Blade_p5_d15-s0.1 peak50%	2.404	3273	16.80	2,6%

Table 6.6: Power variation with the chord distribution

The obtained results indicate that the second configuration is an improvement compared to the baseline configuration, as it requires less Power to generate the same Thrust.

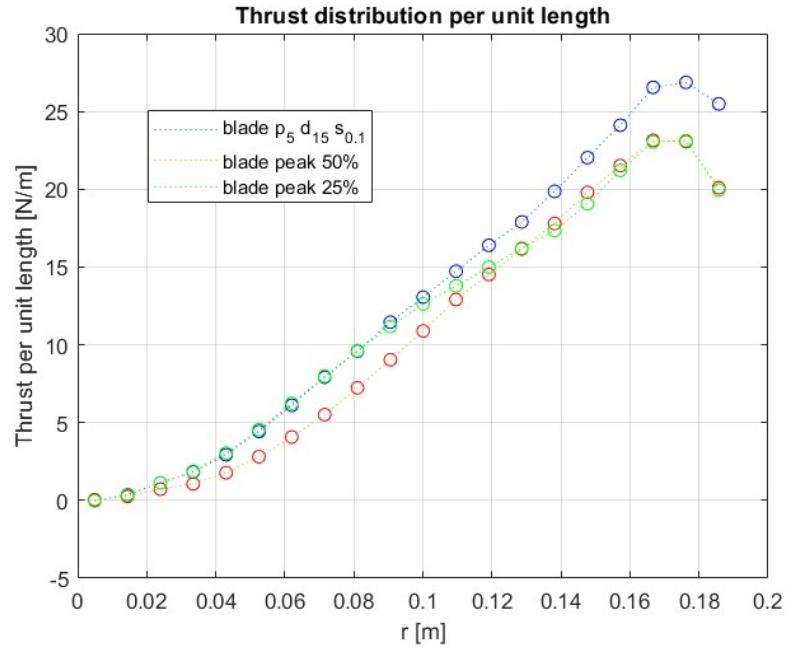


Figure 6.20: Change of thrust distribution with chord distribution

The differences in distribution are minimal in comparison to the baseline one and the change in the local Thrust is primarily concentrated in the final 25% of the blade.

The blade designed with an "elliptical" shape showcases a consistent reduction of Thrust along the blade while the other one exhibits a more uniform distribution. In particular, the first 50% of the blade overlaps the result of the baseline and then aligns with the second configuration in the remaining section.

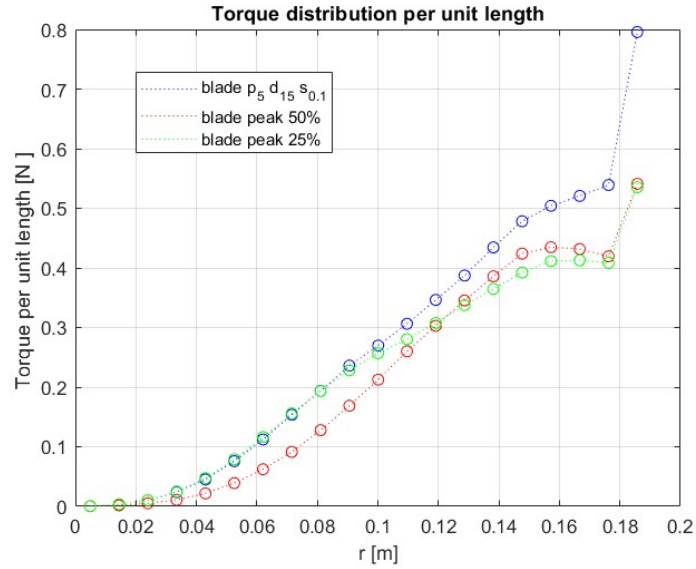


Figure 6.21: Change of torque distribution with chord distribution

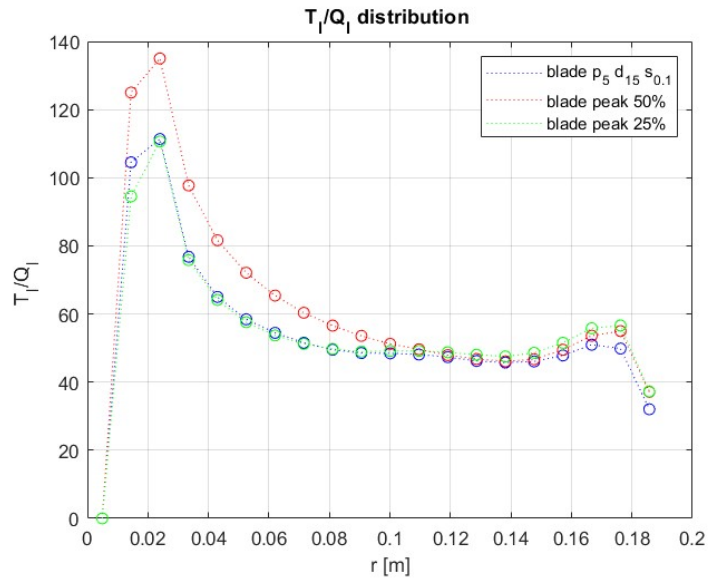


Figure 6.22: Change in T/Q distribution with chord

The result depicted in 6.22 demonstrates that the second configuration mitigates the Drag induced by the tip vortices better than the other configuration.

6.3.2 Qualitative Data

Lastly, in order to identify changes in the tip vortex, a qualitative analysis using the Q-Criterion parameter was carried out:

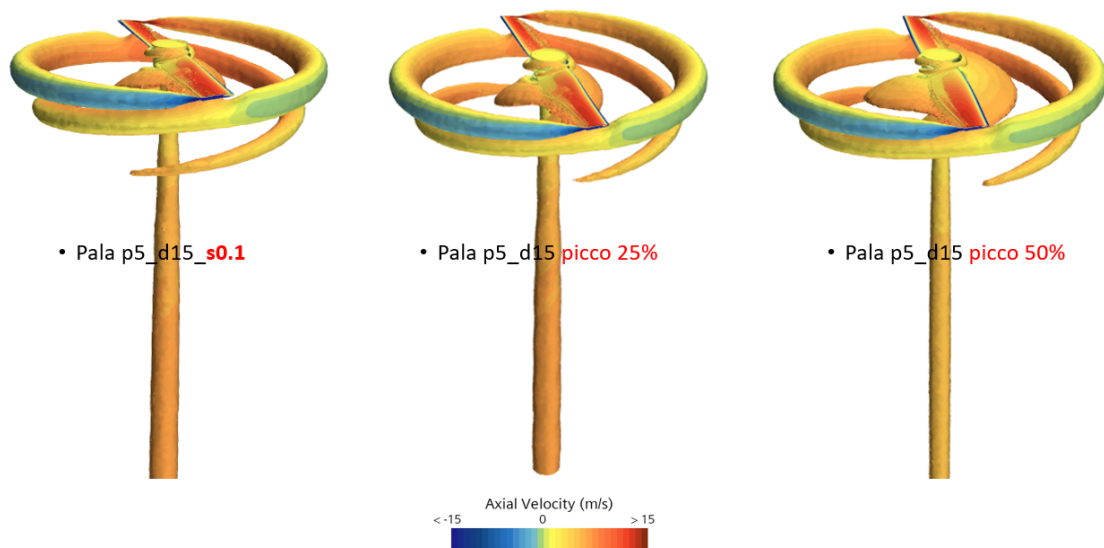


Figure 6.23: Comparison vortex structure Isosurface $Q=5000/s^2$

Through a complete visualization of the vortices, it can be observed that the geometry with a peak at 50% of the structure has a root vortex more extended along the blade but probably less intense.

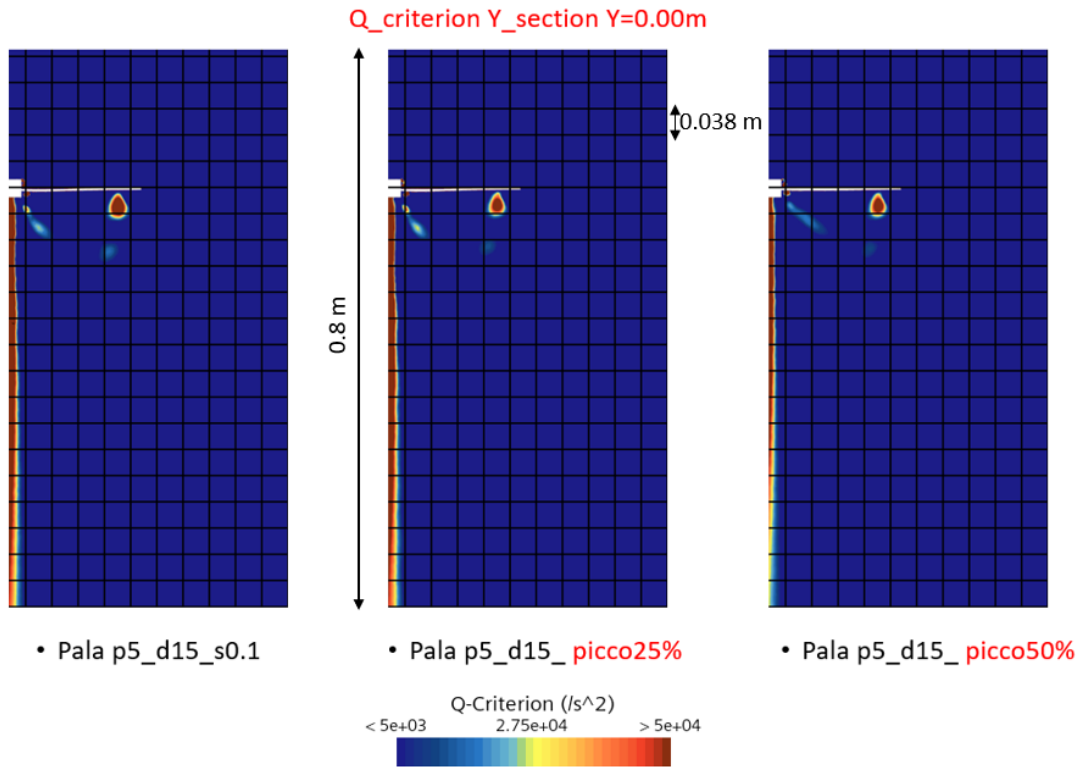


Figure 6.24: Comparison vortex structure $Y=0.0$ m

We can see that the tip vortex belonging to the baseline blade is bigger and has a more extended core compared to the other configurations. Moreover, we can see that the root vortex of the blade with a peak at 25 % has a behavior similar to the baseline blade while the right one shows some differences in both shape and position.

Chapter 7

Conclusion

The objective set by this work thesis has been achieved as the procedure for creating the numerical database is functional and meets the requirements of accuracy, simplicity, and reduced time that we had set for ourselves. The procedure is semi-automatic as it requires some user interactions both in the geometry creation phase and in the run phase, depending on the geometry.

From the initial analyses conducted, we have seen that at least one of the configurations for each geometric modification guarantees an increase in Thrust and Torque without significantly increasing the required Power. In addition, we saw that the **P5-D15-S0.1 geometry with a 25% peak** has a better "efficiency" than the baseline configuration.

After identifying an optimal development range for each geometric parameter, it is now possible to create new geometric configurations while simultaneously changing all geometric parameters.

The next phase of this project will be an expansion of the numerical database and the possibility of introducing a transition model into the procedure, which may be necessary in some configurations.

Bibliography

- [1] Quadricottero News. 2020. URL: <https://www.quadricottero.com/2020/11/drone-agricolo-dji-agras-t16-arriva-in.html> (cit. on p. 1).
- [2] Renato Tognaccini. *Lezioni di AERODINAMICA DELL'ALA ROTANTE*. 2011. URL: http://wpage.unina.it/rtogna/Aerodinamica_del_rotore_2011.pdf (cit. on pp. 3, 8, 9, 15, 43).
- [3] Gaetano Maria Di Cicca. *Appunti Corso fluidodinamica ambiente ed energia, Wing Turbines*. 2022 (cit. on p. 3).
- [4] Manuel Carreno Ruiz. *CFD Simulation of Propellers: Best Practices Analysis*. 2019 (cit. on pp. 11, 13, 17, 24, 26).
- [5] M.Carreño Ruiz; M. Scanavino; D. D'Ambrosio; G. Guglieri; A. Vilard. «Experimental and numerical analysis of hovering multicopter performance in low-Reynolds number conditions». In: *sciencedirect* "128" ("Sep" "2022") (cit. on p. 24).
- [6] *ANSYS FLUENT THEORY GUIDE, Equations for a Rotating Reference Frame*. URL: <https://www.afs.enea.it/project/neptunius/docs/fluent/html/th/node30.htm#fig-stationary-rot> (cit. on pp. 24-26).
- [7] *Simcenter STar-ccm+ wall treatment tutorial*. URL: <Files/Siemens/17.04.008-R8/STAR-CCM+17.04.008-R8/doc/en/online/index.html#page/STARCCMP%2FGUID-478651F1-9901-41B6-8193-3052E3CCE9DB.html%23> (cit. on pp. 26, 27, 33, 34, 36).
- [8] Tordella Daniela. *Appunti Corso Flussi Turbolenti, Parte V*. 2022 (cit. on p. 26).
- [9] Florian R Menter. *Improved two-equation k-omega turbulence models for aerodynamic flows*. Tech. rep. 1992 (cit. on p. 28).
- [10] A. Uranga; P. O. Persson; M. Drela and J. Peraire. “Implicit Large Eddy simulation of transitional flows over airfoils and wings,” 2009 (cit. on pp. 36, 37).

BIBLIOGRAPHY

- [11] L. Z. Wang; C. Y. Guo; Y. M. Su; and T. C. Wu. “A numerical study on the correlation between the evolution of propeller trailing vortex wake and skew of propellers,” 2018 (cit. on pp. 37, 47).
- [12] Andrea manavella. *Validazione delle prestazioni di eliche a bassi numeri di Reynolds tramite analisi CFD e modelli di ordine ridotto*. 2021 (cit. on pp. 44, 58).

Appendix A

Constant Chord Code

```
1 clc
2 clear all
3 close all
4 prompt = {'Passo(pollici):', 'Diametro(pollici):', 'Numero di pale:', '
    solidity:', 'Numero sezioni pala:'};
5 dlgtitle = 'Dati elica';
6 dims = [1 40];
7 definput = {'10', '15', '2', '0.1', '40'};
8 data = inputdlg(prompt, dlgtitle, dims, definput);
9 pollici=str2num(cell2mat(data(1)))/39.37;
10 Diametro=str2num(cell2mat(data(2)))/39.37;
11 Numero_pale=str2num(cell2mat(data(3)));
12 solidity=str2num(cell2mat(data(4)));
13 Numero_sezioni_pala=str2num(cell2mat(data(5)));
14 raggio=Diametro/2;
15 % creazione input_elica
16 x=zeros(Numero_sezioni_pala,5);
17 % posizione radiale
18 dis_corda=linspace(0.5,1,Numero_sezioni_pala)';
19 x(1:end,1)=dis_corda;
20 r=raggio.*x(:,1);
21 % distribuzione corda
22 corda=solidity*raggio*pi/(Numero_pale*0.85);
23 x(:,2)=corda./raggio;
24 %pitch angle
25 beta=rad2deg(atan(pollici./(2*pi*r*0.75)));
26 % pitch angle cambio curva non ottimale
27 x(:,3)=beta;
28 x(1,1)=0;
29 x(1,3)=10;
30 t=linspace(0,1,Numero_sezioni_pala);
```

```
31 y_p=spline(x(:,1),x(:,3),t);
32 plot(t,y_p);
33 x(:,1)=t;
34 x(:,3)=y_p;
35 Imput_elica=matfile("Imput_elica_cordaf_prova.mat","Writable",true);
36 save("Imput_elica_cordafissa_prova.mat","x");
```

Appendix B

Variable Chord Code

```
1      clc
2      clear all
3      close all
4
5      prompt = {'Passo(pollici):', 'Diametro(pollici):', 'Numero di pale:', '
6              solidity:', 'Numero sezioni pala:'};
7      dlgtitle = 'Dati elica';
8      dims = [1 40];
9      definput = {'5', '15', '2', '0.1', '30'};
10     data = inputdlg(prompt, dlgtitle, dims, definput);
11     pollici=str2num(cell2mat(data(1)))/39.37;
12     Diametro=str2num(cell2mat(data(2)))/39.37;
13     Numero_pale=str2num(cell2mat(data(3)));
14     solidity=str2num(cell2mat(data(4)));
15     Numero_sezioni_pala=str2num(cell2mat(data(5)));
16     raggio=Diametro/2;
17     % creazione input_elica
18     X=zeros(Numero_sezioni_pala,5);
19     % posizione radiale
20     dis_rad=linspace(0.9,1,Numero_sezioni_pala)';
21     X(:,1)=dis_rad;
22     r=raggio.*X(:,1);
23     % distribuzione corda
24     f=@(x) 1./sqrt(x);
25     int=integral(f,0.15,1);
26     ctip=(solidity*pi*raggio/Numero_pale)*(1/int)
27     corda=ctip./((X(:,1)));
28     X(:,2)=corda./r;
29     X(1,1)=0;
30     X(1,2)=ctip./raggio;
31     vett=linspace(0,1,Numero_sezioni_pala);
```

```
31 c_p=spline(X(:,1),X(:,2),vett);
32 plot(vett,c_p);
33 X(:,2)=c_p;
34 %pitch angle
35 beta=rad2deg(atan(pollici./(2*pi*r*0.75)));
36 %pitch angle cambio curva non ottimale
37 X(:,3)=beta;
38 X(1,3)=10;
39 y_p=spline(X(:,1),X(:,3),vett);
40 plot(vett,y_p);
41 X(:,3)=y_p;
42 X(:,1)=vett;
43 Imput_elica2=matfile("Imput_elica_cordav_prova.mat","Writable",true)
44 ;
45 save("Imput_elica_VARIABLEI_PROVA.mat","X");
```